


Article

Alkali-Activated Brick Aggregates as Industrial Valorized Wastes: Synthesis and Properties

Abdel Boughriet ^{1,*}, Oscar Allahdin ^{1,2}, Nicole Poumaye ² , Gildas Doyemet ^{1,2}, Grégory Tricot ¹, Bertrand Revel ³, Baghdad Ouddane ¹ and Michel Wartel ¹

¹ Laboratoire Avancé de Spectroscopie Pour les Interactions, la Réactivité et l'Environnement, Université de Lille, CNRS, UMR 8516—LASIRE, 59000 Lille, France; allahdin25@yahoo.fr (O.A.); gildasdoyemet@gmail.com (G.D.); gregory.tricot@univ-lille.fr (G.T.); baghdad.ouddane@univ-lille.fr (B.O.); michel.wartel@univ-lille.fr (M.W.)

² Chaire Unesco «Sur la gestion de l'eau», Laboratoire Hydrosociences Lavoisier, Faculté des Sciences, Université de Bangui, Bangui 908, Central African Republic; poumaye06@yahoo.fr

³ Institut Michel-Eugène Chevreul, Université de Lille, 59000 Lille, France; bertrand.revel@univ-lille.fr

* Correspondence: abdel.boughriet@univ-lille.fr

Abstract: In recent works, many industrial by-products were employed as solid precursors for the synthesis of alkali-activated binders and as alternatives to Portland cement for the immobilization of hazardous, toxic and nuclear wastes. Among industrial wastes, alkali-activated brick was found to be an interesting porous composite for removing very toxic heavy metals (Pb^{2+} , Cd^{2+} , Co^{2+}) and radio-nuclides (Sr^{2+} , Cs^+ , Rb^+) from aqueous solutions. The starting material is very attractive due to the presence of metakaolinite as a geo-polymer precursor and silica for increasing material permeability and facilitating water filtration. The alkaline reaction gave rise to geo-polymerization followed by partial zeolitization. Elemental surface micro-analysis was performed by Scanning Electron Microscopy (SEM) equipped with an Energy-Dispersive X-ray Spectrometer (EDS). The formation of crystalline phases was corroborated by X-ray diffraction (XRD) analysis. Information about ^{29}Si , ^{27}Al and ^1H nuclei environments in crystallized and amorphous aluminosilicates was obtained by ^{29}Si , ^{27}Al and ^1H MAS NMR. ^{27}Al - ^1H dipolar-mediated correlations were investigated by employing dipolar hetero-nuclear multiple quantum coherence (D-HMQC) NMR, highlighting Al–O–H bonds in bridging hydroxyl groups (Si–OH–Al) that are at the origin of adsorptive properties. Aqueous structural stability and cationic immobilization characteristics before and after material calcination were investigated from acid-leaching experiments.

Keywords: brick; composite; geo-polymer; zeolite; ALOSi angle; radioactive elements immobilization; scanning electron microscopy; 1D and 2D MAS NMR



Citation: Boughriet, A.; Allahdin, O.; Poumaye, N.; Doyemet, G.; Tricot, G.; Revel, B.; Ouddane, B.; Wartel, M. Alkali-Activated Brick Aggregates as Industrial Valorized Wastes: Synthesis and Properties. *Ceramics* **2023**, *6*, 1765–1787. <https://doi.org/10.3390/ceramics6030108>

Academic Editors: Kinga Korniejenko and Marek Nykiel

Received: 7 July 2023

Revised: 2 August 2023

Accepted: 7 August 2023

Published: 14 August 2023



Copyright: © 2023 by the authors. Licensee MDPI, Basel, Switzerland. This article is an open access article distributed under the terms and conditions of the Creative Commons Attribution (CC BY) license (<https://creativecommons.org/licenses/by/4.0/>).

1. Introduction

Human activities, such as fossil fuel burning, deforestation and cement production, have contributed strongly to the excessive emission of carbon dioxide into the atmosphere and the acceleration of global-warming phenomena. In order to limit climate change, more efficient policy actions towards decarbonization must be undertaken urgently [1]. Among them, a better efficiency/control of extraction procedures and management of non-renewable natural resources and incentive re-using/recycling and valorising of industrial (by-)products have to be encouraged to diminish substantially environmental degradation and ensure environmental preservation and sustainability.

Portland cement is an industrial low-cost product that has been used for many years as a stabilization/solidification matrix for immobilizing low- and intermediate-level radioactive liquid wastes [2]. However, radio-nuclides are found to be generally difficult to stabilize within cement matrices [3], because these latter are prone to have structural and/or chemical degradations in contact with aggressive media or at high temperatures.

The generation of micro-cracks in solidification matrices (concretes) may cause, with time, radioactive leaching and severe contamination in disposal sites, thereby preventing safe land disposal. To improve the physical and chemical stability of the matrix and limit radioactive leaching in aqueous aggressive media, cementitious materials, such as blast furnace slag, fly ash and metakaolin, have been proposed as promising alternatives to Portland cement for the immobilization of hazardous, toxic and nuclear radio-elements, such as cesium, strontium, cobalt and europium [4–14], and by employing them either alone or combined with other solid aluminosilicate precursors [3]. It is worth noting that, contrary to normal concrete, alternative cementing systems based on aluminosilicate polymers or geo-polymers are characterized by a lack of calcium and, thereby, would not suffer from effects such as carbonation or acid leaching after stabilization/solidification [15].

In order to enrich or separate radio-nuclides, the adsorption and ion exchange method remains the best (efficiently and economically) remediation technique due to a facile large-scale production, much lower operating costs and, above all, easier industrial operability. Many inorganic ions exchange materials and multi-functional core-shell adsorbents exhibit high adsorption capacity and excellent selectivity in the removal of nuclides from solutions [16,17]; but, these materials presented relevant disadvantages and difficulties in practical/industrial applications, such as (i) products costs; (ii) complicated synthesis processes consisted of two or more reaction steps, rendering adsorbent preparation relatively costly and time-consuming; and mostly, (iii) small particulate sizes which are not suitable for carrying out large-scale water treatment (in dynamic adsorption) or separating powdered particles from the liquid phase. In contrast, the heterogeneous surface behavior of mixed materials (or composites) contributed to improving adsorption capacity, permeability and filtration, especially owing to the possibility of obtaining larger particle sizes which are more adapted to column experiments [18,19]. Recent studies thus revealed remarkable advantages of using geo-polymer-zeolite-A composites for immobilizing radioactive wastes [20]. Analogically with previous works on the synthesis of zeolite-geo-polymer composites using industrial solid wastes [21], a zeolite-geo-polymer composite was prepared in the lab by proceeding to an alkaline activation of a metakaolin-rich brick.

The aim of this paper was to review the chemical, mineralogical and micro-structural properties of alkali-activated brick as a promising matrix for radio-nuclides immobilization in the perspective of large-scale applications.

In the first part of this work, a few comments were made about the different reaction steps of the “brick-composite” synthesis.

In the second part, chemical and mineralogical analyses of alkali-activated brick aggregates were performed by using an environmental scanning electron microscope (ESEM) equipped with an energy-dispersive X-ray spectrometer (EDS), and their crystalline characteristics were determined by using X-ray diffraction.

In the third part, the generation of crystallized and amorphous aluminosilicates was evidenced and quantified by means of ^{29}Si and ^{27}Al MAS NMR spectroscopy. Information about ^1H nuclei environments was obtained by ^1H MAS NMR. ^{27}Al - ^1H dipolar-mediated correlations were investigated by employing dipolar hetero-nuclear multiple quantum coherence (D-HMQC) NMR with the aim of highlighting the occurrence of Al-O-H bonds and their implication in bridging hydroxyl groups (Si-OH-Al).

In the fourth part, the aqueous structural stability and cationic immobilization characteristics of the brick-based composite before and after its calcination were investigated from acid-leaching experiments and analytical data were discussed.

2. Materials and Methods

2.1. Materials Preparation and Making Cost

The raw material used in the experiments was obtained from a brick made locally by craftsmen in the Bangui region (Central African Republic). This brick contains mainly quartz (60–65 w%) and metakaolinite (20–26 w%) and, to a lesser extent, iron oxide/hydroxide, illite and titanium dioxide [22]. Before alkaline treatment, the brick was broken into grains

and sieved with sizes ranging from 0.7 to 1.0 mm. Second, brick pellets were treated with sodium hydroxide according to the following optimized synthesis conditions [23]: 10 g of Bangui brick reacted in 40 mL of a diluted NaOH solution ($0.6 \text{ mol}\cdot\text{L}^{-1}$) at room temperature for one night under a slow shaking at a speed of 120 rpm. This procedure was afterward followed by a fixed-temperature increase of the mixture at $90 \text{ }^\circ\text{C}$ for a constant reaction time of six days. Finally, the recovered grains were rinsed several times with MilliQ water and dried at $90 \text{ }^\circ\text{C}$ for 24 h.

Making cost of synthesized composite: Briefly, a raw brick which was provided by African craftsmen (in the Central African Republic) and used here as starting material weighed about 5 kg, and its price is 75 CFA (i.e., 0.11 Euro; 1 CFA = ~ 0.0015 Euro); while solid sodium hydroxide which was provided by local soap factories and used here as reagent cost 30,000 CFA/25 kg (i.e., 45 Euros). Knowing that 4 liters of a NaOH solution at a concentration of $\sim 0.6 \text{ mol}\cdot\text{L}^{-1}$ were necessary to treat 1 kg of ground brick, the authors estimated the cost for synthesizing 1 kg of adsorbent at ca 0.20 Euro (without taking into account labor costs, which are very low in this country). Hence, the low making cost of the brick-based composite should enable its use as a good low-cost adsorbent for radioactive wastewater treatment.

As for the NH_4^+ -saturated alkali-brick, an ion-exchange reaction between Na^+ ions in brick frameworks and NH_4^+ ions in the aqueous phase was carried out by mixing 1 g of alkali-brick grains (diameter 0.7–1.0 mm) with 100 mL of an NH_4Cl solution ($2 \text{ mol}\cdot\text{L}^{-1}$). The suspension was shaken gingerly for 24 h in a thermostatic orbital shaker. The resulting brick grains were afterward filtered, and the filtration operation was repeated three times with the aim of ensuring a total exchange of extra-framework sodium with ammonium. Finally, brick grains were rinsed several times with Milli-Q water and dried at $70 \text{ }^\circ\text{C}$ for 24 h.

2.2. Chemicals

All chemicals employed in the experiments were analytical grades. Sodium hydroxide, ammonium chloride and hydrochloric acid were supplied by DISLAB (Paris, France).

2.3. Electron Microscopy Analysis

Micrographs of representative specimens of the brick before and after chemical treatment were recorded by using an environmental scanning electron microscope equipped with an Energy Dispersive X-Ray Spectrometer EDS X flash 3001 (ThermoFisher Scientific, Courtaboeuf, France). EDS measurements were carried out at 20 kV at low vacuum (1.00 Torr), and the maximum pulse throughput was 20 kcps. Different surface areas ranging from 0.12 to 0.50 mm^2 were targeted on alkali-brick grains and examined by ESEM/EDS. For that, a narrow beam scanned selected areas of brick pellets for chemical analysis. Atomic quantifications and mathematical treatments were undertaken using QUANTA-400 software in order to determine the averaged elemental composition of the surface brick and to detect chemical/elemental variability.

2.4. X-ray Diffraction Analysis

XRD patterns were conducted at room temperature in a Bruker D8 Advance diffractometer (Evry, France) using Ni-filtered $\text{CuK}\alpha$ radiation (40 kV, 40 mA). Samples were scanned with a step size of 0.02° and a counting time of 0.5 s per step.

2.5. MAS NMR Analysis

The ^{29}Si MAS-NMR experiments were acquired at 79.5 MHz on a Bruker 9.4 T spectrometer (Palaiseau, FR) equipped with a Bruker 7.0 mm MAS probe operating at a spinning frequency (ν_{rot}) of 4 kHz. The ^{29}Si MAS-NMR spectra were recorded with a pulse length of $5 \mu\text{s}$ ($\pi/2$ flip angle), 256 transients, and a recycle delay (rd) of 30 s. This short rd value was possible because of the presence of paramagnetic species (as iron(III) oxides/hydroxides) homogeneously distributed within the brick matrix. The ^{29}Si MAS-NMR spectra were

decomposed using the Gaussian/Lorentzian model of the dmfit software (version 2.0) [24]. The ^1H , ^{23}Na and ^{27}Al MAS-NMR spectra were recorded at 800, 211.7 and 208.5 MHz, respectively, on a Bruker 18.8 T spectrometer equipped with a Bruker 3.2 mm CP-MAS probe operating at a ν_{rot} of 20 kHz. The ^{23}Na ($I = 3/2$) MAS-NMR experiments were recorded with a pulse length of 1 μs ($\sim\pi/5$ flip angle), 1024 transients, and a recycle delay of 2 s. The ^{27}Al ($I = 5/2$) MAS-NMR spectra were obtained with a pulse length of 1 μs ($\sim\pi/10$ flip angle), 1024 transients, and a recycle delay of 2 s. The ^1H MAS-NMR experiments were recorded with a $\pi/2$ pulse length of 3.5 μs , 128 transients and a 5 s rd using the DEPTH sequence in order to suppress the signal coming from the measurement probe. The presence of Al–O–H bonds was investigated by correlation NMR with the $^{27}\text{Al}(^1\text{H})$ dipolar heteronuclear multiple quantum coherence (D-HMQC) NMR technique [25,26]. The 2D maps were recorded under rotor-synchronized conditions at 18.8 T with 2048×40 acquisition points. Each direct slice was recorded with ^{27}Al and ^{29}Si π pulses of 16 and 10 μs , 1024 transients, a rd of 2 s and a 2 ms SR4_1^2 re-coupling scheme. All the ^{29}Si , ^1H , ^{23}Na and ^{27}Al chemical shifts were referenced as 0 ppm to TMS, TMS, NaCl solution (1 M), and $\text{Al}(\text{NO}_3)_3$ solution (1 mol.L $^{-1}$), respectively. It is noteworthy that the spectra acquired at high field (^1H , ^{23}Na and ^{27}Al) were recorded on similar sample mass (40 mg) in order to compare the peak intensities on the different NMR spectra.

2.6. Acid Leaching Tests

Leaching of different elements (Si, Al and Na) was carried out on alkali-brick samples (mass of composite: 500 mg) in different HCl solutions (volume of leachant: 50 mL) with pH values ranging from 0.39 to 4.83 at room temperature. Under similar experimental conditions, leaching of radioactive elements (Cs and Rb) and Si, Al and Na was carried out on Cs (or Rb)-doped alkali-brick in a 0.01 M HCl solution (pH~2). Each collected leachate was vacuum filtered through a 0.45 μm membrane filter. The concentrations of leached elements present in these leachates were determined by using an inductively coupled plasma optical emission spectrometer (ICP–OES, model 5110 VDV, Agilent Technologies).

3. Results and discussion

3.1. Synthesis Process

During the reaction course of brick-composite synthesis, the metakaolinite mineral initially present in the raw brick was dissolved in an alkali medium by forming sodium poly/mono silicates and sodium aluminates intermediately; these ionic species were subsequently polymerized into gel-state sodium alumino-silicate(s) which impregnated insoluble brick pellets. This polymerization/impregnation was followed by an induction period during which nucleation/crystallization took place at the surfaces of unreacted brick grains (mainly quartz) [27,28]. These authors [27,28] also stated that the presence of a high amount of quartz (60–65 w%) as a “secondary matrix” in brick composite contributed to facilitating the flow of inlet solutions through fixed-bed columns. Note that alkali brick had recently been assimilated to an adsorptive membrane prepared from blended zeolites into a layered geo-polymer-quartz matrix [29]. This mixed material might be considered as a surface composite membrane possessing a dual function of adsorption and filtration: with zeolitic/geo-polymeric aggregates favoring adsorption capacity, while quartz matrix allowing mostly low operating pressure and high permeability flux [29].

3.2. Microscopic and Crystalline Studies

3.2.1. Microscopic (ESEM/EDS) Analysis

ESM analysis of raw brick revealed the presence of porous and non-textural surfaces with major fissures and cracks, except for quartz crystals [22,30]. In addition, elemental (ESEM/EDS) analysis indicated the presence of: (i) silicon (Si), aluminum (Al), oxygen (O) and iron (Fe) as major elements; and (ii) titanium (Ti), magnesium (Mg), potassium (K), and calcium (Ca) as minor elements. Some of these elements were found to be distributed across brick surfaces with apparent localization, evidencing the existence of mainly SiO_2 (as quartz)

and alumino-silicate (as metakaolinite) and, to a lesser extent, iron oxides/hydroxides and rutile [22].

As for alkali-activated brick aggregates, ESEM analysis revealed that the morphological aspect of the treated brick was changed significantly into aggregated cubic and spherical shapes (Figure 1). The size of these new specimens varied from 7 μm to 10 μm for cubic ones and from 3 μm to 6 μm for spherical ones. Cubic crystals were found to be comparable with those observed previously for the A-type zeolite [31,32], while spherical shape crystals were morphologically similar to those reported in the literature for zeolite NaP [33–35].

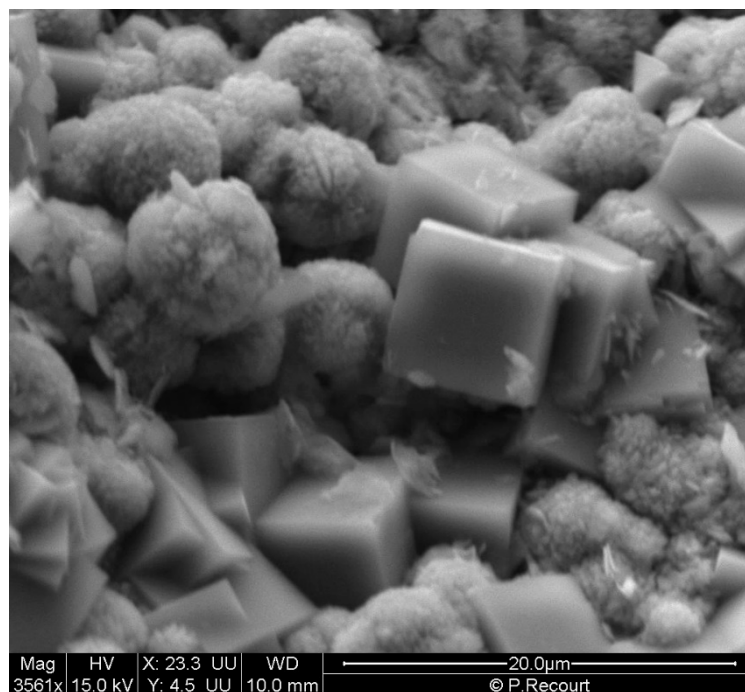


Figure 1. ESEM image of brick-composite specimens.

The spatial distribution of the framework elements Al, Fe, Na and Si is displayed in Figure 2. The ESEM/EDS mapping procedure gives the color overlay shown in this Figure, where the elemental distributions for Al, Fe, Na and Si are represented in red, green, yellow, and blue, respectively. Element distribution images indicate a positive correlation between Al, Si and Na (Figure 2B) due to the presence of sodic alumino-silicates as Na-zeolites. Conversely, there is a negative correlation between sodium and silicon in Si-rich zones which are composed of quartz crystals (in blue regions of the reconstituted image; see Figure 2A). Note as well the presence of micro-specimens of TiO_2 (rutile) in the elemental distribution for titanium; see Figure 2B.

Quantitative ESEM/EDS analysis permitted us to show that the elemental composition of cubic and spherical specimens corresponded well to those of low-silica zeolites with atomic ratios of Si/Al close to 1. Indeed, the atomic percentage of aluminum and silicon were 14.97 ± 2.05 atomic % and 16.12 ± 1.46 atomic %, respectively, which led to an averaged atomic ratio Si/Al of 1.08 (or Al/Si = 0.926). As for sodium, we found: 14.77 ± 2.67 atomic %. The presence of high amounts of sodium on the surfaces of cubic and spherical particles confirmed the presence of sodic zeolites.

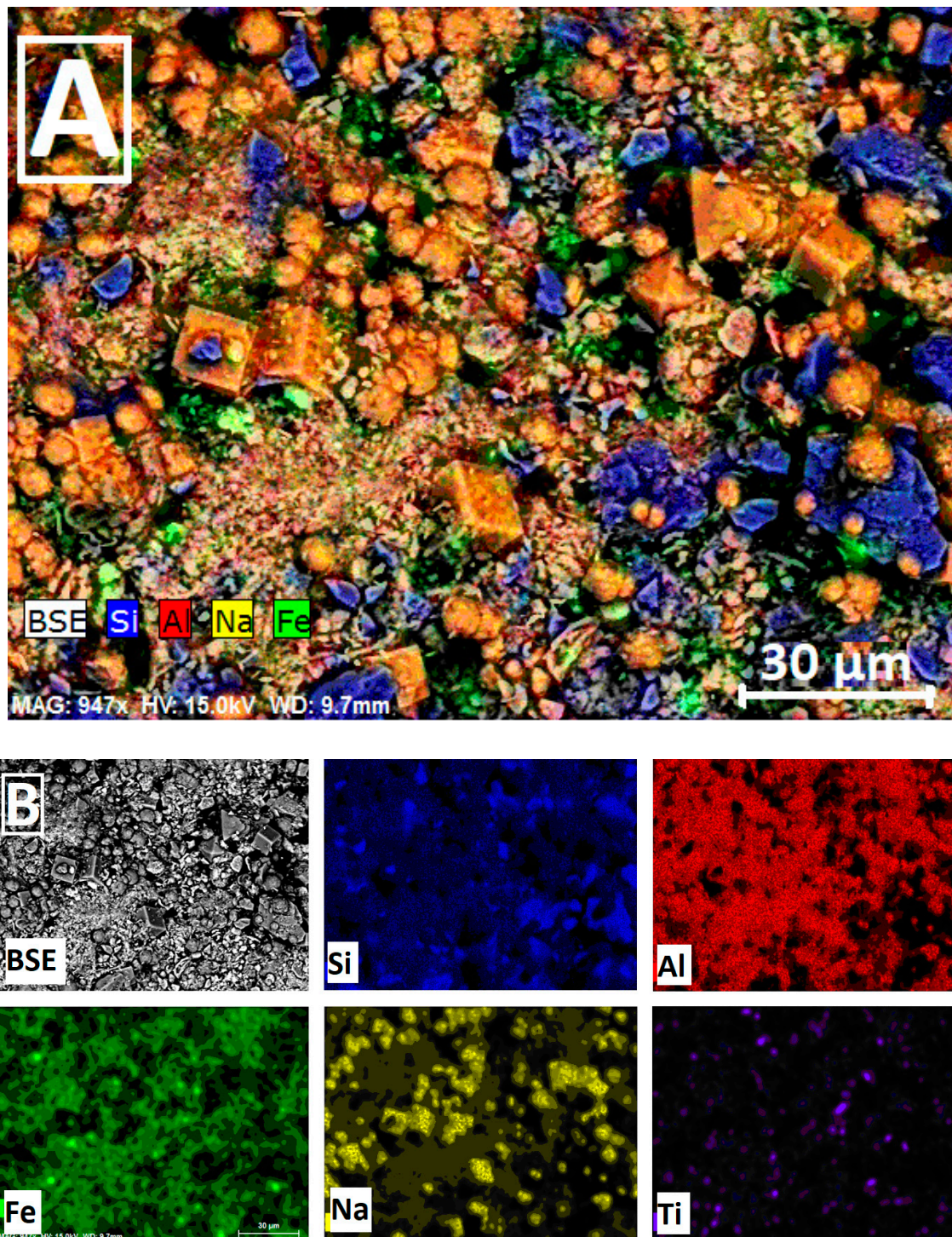


Figure 2. Reconstituted ESEM/EDS mapping image of alkali-activated brick aggregates (A); Spatial distribution of the framework elements Al, Fe, Na, Si and Ti (B). BSE: Energy Selected Backscatter.

3.2.2. X-ray Diffraction (XRD) Analysis

Figure 3a displays the XRD patterns of raw-brick powder. XRD analysis revealed that the material contains quartz as the principal crystalline mineral and, to a lesser extent, illite and rule. In what follows, minerals were identified on the basis of 2θ reflection angles and “hkl” Miller indices (“hkl” indices are given in the parenthesis).

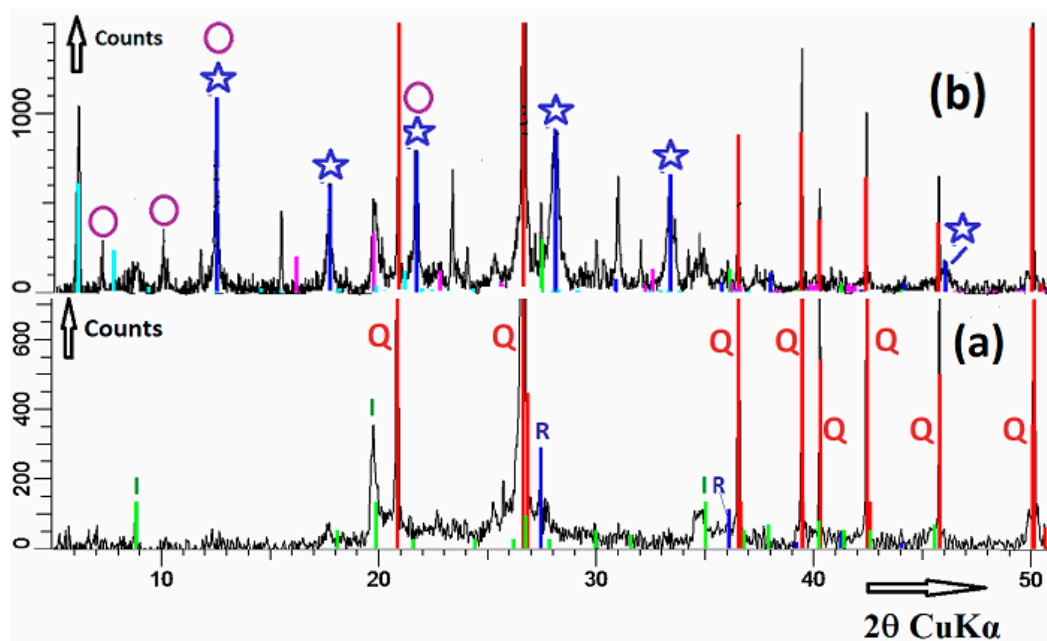


Figure 3. XRD patterns of raw brick (a) and alkali brick (b): I, illite; Q, quartz; R, rutile; (☆), NaP zeolite; (○), LTA zeolite.

Quartz: 20.9° (100); 26.6° (011); 36.5° (110); 39.5° (102); 40.3° (111); 42.4° (200); 45.8° (201); and 50.1° (112) [ICSD Collection Code: 89276]. Illite: 8.8° (001), 17.9° (004), 19.8° (021), and 34.3° (034) [ICDD (International Centre for Diffraction data): 00-009-0343]. Rutile: 27.4° (110) and 36.1° (101) [ICSD Collection Code: 168140].

Figure 3b displays the XRD patterns of alkali-brick powder. Compared to the XRD patterns of raw brick, one can observe new XRD signals in addition to those ascribed to quartz, illite and rutile. These reflections were attributed to zeolites LTA and NaP.

LTA: 7.2° (200), 10.2° (220), 12.5° (222) and 21.7° (600 and 442) [36]. NaP: 12.5° (101 and 110), 17.7° (200 and 002), 21.7° (211, 112 and 121), 28.1° (310, 301, and 103), 33.4° (132, 123, 231, 213, 312, and 321) and 46.1° (134) [36].

3.3. Solid MAS MNR Study

In the past, Magic Angle Spinning (MAS) Nuclear Magnetic Resonance (NMR) spectroscopy was successfully used for providing relevant information about structure changes, chain lengths and elements ratios of (three-dimensional) geo-polymeric gels present in alkali slag and fly ash as aluminosilicates dominated (Si + Al) industrial by-products [37]. This led us to undertake detailed NMR analyses of alkali brick to gain a comprehensive insight into the different ^{29}Si , ^{27}Al , and ^1H atomic environments constituting the heterogeneous nature of alkali-activated brick. Ammonium chloride (NH_4Cl) was used as a probe for bringing information about the characteristics and mobility in brick-composite frameworks by means of ^1H MAS NMR [1D ^1H and 2D $^{27}\text{Al}(^1\text{H})$ D-HMQC].

Moreover, before undertaking the analysis of NMR data, it was important to mention that it was observed no noticeable broadenings of NMR peaks related to paramagnetic NMR effects arising from the interactions of nuclear spins (^1H , ^{23}Na , ^{29}Si or ^{27}Al atoms) with unpaired d electrons (Fe(III)). This could result from the presence of too-low Fe contents detected in alkali-brick samples by ESEM/EDS (ranging from 0.2% to 0.7%), suggesting that resonating nuclei detected were certainly located far from paramagnetic centers.

3.3.1. ^{29}Si MAS NMR

Figure 4 displays solid-state MAS NMR data for ^{29}Si nuclei in alkali brick before and after different chemical treatments. The ^{29}Si MAS NMR spectrum of an alkali-brick sample indicated several signals (ranging from -70 ppm to ~ -135 ppm), which characterized

the resonances of framework silicon atoms in $Q^4(mAl)$ type environments with m varies between 0 and 4. Note globally that in the ^{29}Si MAS NMR spectra, the relatively high intensity of resonances in the range (-84) – (-90) ppm reflected the importance of Al-rich structural units inside brick frameworks.

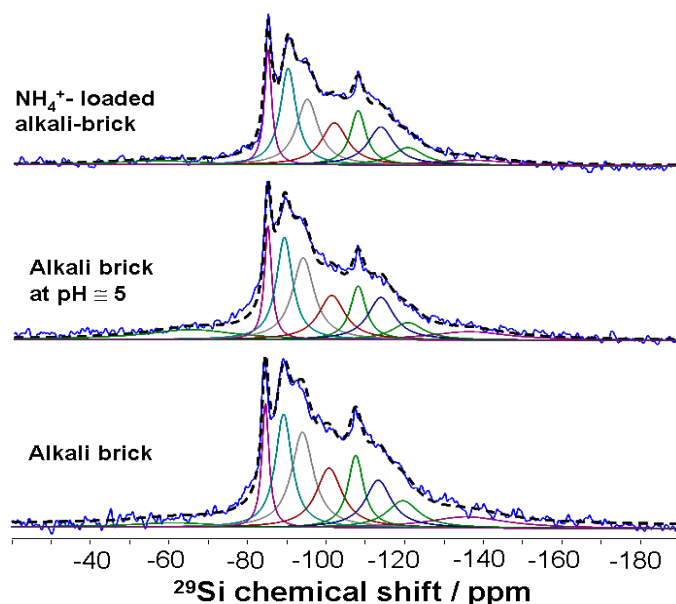


Figure 4. ^{29}Si MAS NMR spectra of alkali brick before and after different chemical treatments. De-convoluted spectra were obtained by employing the dmfit software [24].

In order to facilitate the interpretation of ^{29}Si MAS NMR data, the experimental ^{29}Si MAS NMR spectra were de-convoluted (Figure 4). Components were identified through the de-convolution of the spectra into individual Gaussian/Lorentzian peaks representing different silicon centers: $Q^n(mAl)$ with n and m capable of varying from 0 to 4. The de-convolution criterion followed at best published ^{29}Si NMR results relative to the different chemical environments surrounding the silicon nucleus belonging to the following compounds [38–42]: (i) zeolites NaA and NaP; (ii) aluminosilicate gels produced during the alkali activation of metakaolin; and (iii) quartz as an unreacted mineral present in the starting material. It is noteworthy to mention that other un-reacted starting materials such as illite and biotite (which are nevertheless present at low levels in the analyzed material) would also contribute to the resonances detected and, as a consequence, lead to some degree of error in the decomposition of the ^{29}Si MAS NMR spectra.

The de-convolution of the ^{29}Si MAS NMR spectrum of alkali brick revealed a series of peaks at -84.5 , -89.2 , -94.0 , -100.7 , -107.5 , -113.3 and -119.5 ppm (± 0.3 ppm), see Figure 4 and Table 1. The NMR line at -89.2 ppm corresponded well to the chemical shift of Si atoms in $Q^4(4Al)$ sites in NaA zeolite [39] and NaP zeolite [41]. The NMR resonances at -94.0 and -100.7 ppm were close enough to those detected for NaP zeolites by Criado and co-workers [41]: These authors ascribed them to silicon tetrahedra surrounded by a certain coordination number of ^{27}Al atoms ranging from 3 to 1, respectively ($Q^4(1-3Al)$). As a whole, the NMR peaks at -94.0 and -100.7 ppm might certainly be due to $Si(OSi)(OAl)_3$, $Si(OSi)_2(OAl)_2$ and/or $Si(OSi)_3(OAl)_1$, respectively. As for the particular NMR peak at -84.5 ppm, it was associated with the presence of sodalite-type $Q^4(4Al)$ units in brick gel [41,43]. The -84.5 ppm signal was comparable enough to that observed previously for alkaline inorganic polymers generated through the alkaline activation of pure metakaolinite [40]. Such polymers exhibited additional peaks at around $-87/-89$ ppm and -94 ppm, which were superimposed on those of NaA and NaP zeolites [40]. These resonances were, therefore, assigned partly to tetrahedrally coordinated and fully polymerized (Q^4) silicon nuclei surrounded by m AlO_4 tetrahedra and associated with the chemical ^{29}Si environments in alkali-activated metakaolin. Indeed, according to Fernandez-Jiménez

and co-workers [40], the ^{29}Si MAS-NMR spectrum of metakaolin illustrating its chemical transformation into an alumino-silicate gel during alkaline activation exhibited three well-defined signals at around -84.6 , -89 , and -94 ppm. These chemical shifts were similar enough to those obtained for chemically bonded ceramic/cementitious materials of alkali-activated metakaolin, revealing a wide signal with several overlapped peaks, and their de-convolution indicated the presence of $\text{Q}^4(4\text{Al})$, $\text{Q}^4(3\text{Al})$ and $\text{Q}^4(2\text{Al})$ units at -84 , -89 and -92 ppm, respectively [44,45]. Note further that the relatively high intensity of the -89.2 ppm signal observed in Figure 4 was explained by the fact that zeolites NaA and NaP contributed strongly to this signal. The -89.2 ppm resonance, which was associated with $\text{Q}^4(4\text{Al})$ units in zeolites NaA and NaP, was assigned to the resonance of ^{27}Al nuclei in double four-membered rings (with sodalite cages) of brick zeolites [38,40]. It was also interesting to note that, after the adsorption of NH_4^+ ions onto alkali brick, the ^{29}Si sites were somewhat better distinguished and, hence, the different MAS NMR lines could be more easily quantified (Figure 4 and Table 1).

Table 1. De-convolution data was obtained for the ^{29}Si MAS NMR spectra of alkali-activated brick before and after slight acidification (pH 5) and ammonium treatment.

^{29}Si MAS NMR (de-Convolution)	$\text{Q}^4(4\text{Al})$ (in gel)	$\text{Q}^4(4\text{Al})_{\text{ze}}$ and $\text{Q}^4(3\text{Al})_{\text{gel}}$	$\text{Q}^4(2\text{Al})$	$\text{Q}^4(2\text{Al})$ and/or $\text{Q}^4(1\text{Al})$	$\text{Q}^4(0\text{Al})$	$\text{Q}^4(0\text{Al})$	$\text{Q}^4(0\text{Al})$
Alkali-activated brick							
$\delta_{\text{iso}}/\text{ppm}$	-84.5	-89.2	-94.0	-100.7	-107.5	-113.3	-119.5
FWHM/ppm	2.2	5.1	6.7	8.0	4.8	8.0	9.8
Relative intensity(%)	9.2	19.5	22	16	11	13	9.2
Alkali-activated brick (pH 5)							
$\delta_{\text{iso}}/\text{ppm}$	-84.5	-88.7	-93.5	-100.7	-107.5	-113.3	-120.7
FWHM/ppm	2.2	5.0	6.7	8.2	4.8	8.0	9.8
Relative intensity(%)	11	20	23	14	11	14	7
NH_4^+-loaded alkali-activated brick							
$\delta_{\text{iso}}/\text{ppm}$	-84.5	-89.7	-94.6	-101.5	-107.5	-113.3	-120.2
FWHM/ppm	2.2	4.9	6.7	8.0	4.8	8.0	9.8
Relative intensity(%)	11	21	20	15	12	13	8

The chemical shift (δ_{iso}), full width at half maximum (FWHM) and relative peak intensity (I%) are given with errors of ± 0.3 ppm, 0.4 ppm and 1.0%, respectively.

In addition, it was found that by using X-ray diffraction, brick quartz was apparently not (or barely) attacked by alkaline treatment [46]. A resonance at -107.7 ppm in the ^{29}Si MAS NMR spectrum of alkali brick (Figure 4) revealed $\text{Q}^4(0\text{Al})$ units in quartz [47,48]. The low intensity of this signal in our ^{29}Si MAS-NMR experiments was explained by the relatively short recycle delay. This delay did not allow for a full relaxation of the quartz signal, leading to an under-estimated intensity compared to the other ^{29}Si resonances. In addition to the $\text{Q}^4(0\text{Al})$ signal corresponding to the quartz mineral, other $\text{Q}^4(0\text{Al})$ signals were observed at -113.3 and -119.5 ppm (see Figure 4 and Table 1). According to the literature, these peaks could be attributed to highly polymerized amorphous silica structures generated through condensation of silicate tetrahedrons during metakaolin geo-polymerization, thus leading to an increasing fraction of $\text{Q}^4(0\text{Al})$ [45,49].

From ^{29}Si NMR data (see Table 1), it was possible to estimate the silica contribution of un-reacted aluminosilicate gel, $\text{Si}(\text{gel})\%$, to the overall ^{29}Si MAS NMR peak of “zeolitized” brick-metakaolinite from the expression (in atomic %):

$$\text{Si}(\text{gel})\% = \frac{I\%(\text{gel})}{I\%(\text{gel}) + I\%(\text{zeolites})} \times 100\% \quad (1)$$

where $I\%(\text{gel})$ and $I\%(\text{zeolites})$ represent the intensity percentages of ^{29}Si resonances ascribed respectively to aluminosilicate gel and zeolites in the ^{29}Si MAS NMR spectrum of alkali-activated brick. Note that in this calculation: (i) we considered only the areas of the signals at -84.5 , -94.0 and -100.7 ppm, which were assigned to $\text{Q}^4(4\text{Al})$, $\text{Q}^4(2\text{Al})$, $\text{Q}^4(2-1\text{Al})$ units in aluminosilicate gel(s) [41,43]; and (ii) we did not take into account polymerized amorphous silica structures with $\text{Q}^4(0\text{Al})$ (i.e., the ^{29}Si NMR peaks at -113.3 ppm and -119.5 ppm, see Table 1). We found at least 70 atomic % of ^{29}Si nuclei present in the “aluminosilicate” gel(s) of the partially zeolitized brick.

From the quantification of the different $\text{Q}^4(\text{mAl})$ species of modified bricks (see Table 1), Engelhard’s formula (Equation (2)) was used here to estimate the Si/Al molar ratio in aluminosilicates at composite surfaces [50].

$$\frac{\text{Si}}{\text{Al}} = \frac{\sum_{m=0}^{m=4} \text{Q}^4(\text{mAl})}{\sum_{m=0}^{m=4} \frac{m}{4} \cdot \text{Q}^4(\text{mAl})} \quad (2)$$

We found an atomic Si/Al ratio ranging approximately from 1.35 to 1.53. These Si/Al values result from macroscopic chemical (NMR) analysis of silicon elements in the material. Conversely, the ESEM/EDS results obtained corresponded rather to microscopic chemical analysis of brick surfaces (see Section 3.2.1 and Table 2) and cannot be directly compared with NMR data. For instance, by using the ESEM/EDS technique, we instead found the following atomic Si/Al ratios: (i) $\text{Si}/\text{Al} = 1.58 \pm 0.16$ for large, targeted zones of surface alkali-brick recovered with both quartz and zeolites; (ii) 1.22 ± 0.08 for targeted zeolites-rich zones; and (iii) 1.11 ± 0.07 for specific zeolitic specimens. As a consequence, it could be stated from ESEM/EDS investigations that alkali-brick grains were mostly coated with zeolitic frameworks (NaA and NaP) (as shown in Figures 1 and 2) and would barely be coated with alumino-silicate gel(s) (as detected macroscopically by NMR). To our mind, composite gels ought to be more present in layer(s) beneath zeolitic coatings.

Table 2. Elemental (ESEM/EDS) analyses of alkali-activated brick aggregates were performed at different magnifications.

ESEM/EDS		O	Na	Mg	Al	Si	K	Ca	Ti	Fe
Alkali-brick surface (global) ^a	At. %	60.98	9.08	0.37	10.97	17.29	0.56	0.07	0.18	0.50
	σ	0.89	0.25	0.02	0.68	0.60	0.25	0.03	0.05	0.18
Targeted zeolitic zones ^b	At. %	53.66	9.56	0.91	14.89	18.24	1.00	0.41	0.13	0.79
	σ	1.71	5.35	0.22	1.75	3.33	1.39	0.55	0.03	0.53
Zeolite specimens targeted ^c	At. %	50.75	12.37	0.55	16.61	18.38	0.25	0.44	0.07	0.44
	σ	6.29	2.07	0.16	2.65	1.48	0.03	0.39	0.02	0.24

^a see Figure S3A; ^b see Figure S3B; ^c see Figure S3C.

3.3.2. ^1H and ^{23}Na MAS NMR

Figure 5 displays solid-state MAS NMR data for ^1H nuclei in fine alkali-brick grains in which brick metakaolinite was thoroughly transformed into zeolites. The ^1H MAS NMR spectrum of zeolitized brick exhibits an intense signal spreading between ~ 2 ppm and ~ 9 ppm (Figure 5A). In this chemical shift range, it can be seen a principal resonance at 4.6 ppm accompanied by weak and sharp peaks at 4.2 ppm and 3.7 ppm. All these ^1H NMR

resonances were ascribed to a wide distribution of various water molecules and proton species taking place in the zeolitic frameworks (α and β cages) of zeolitized brick [22]. As for the badly resolved resonances in the $\delta^{1\text{H}}$ range of $\sim 1\text{--}3$ ppm, they were either non-acidic or weakly acidic hydroxyl groups. These were assigned to isolated silanol/aluminol protons in brick minerals.

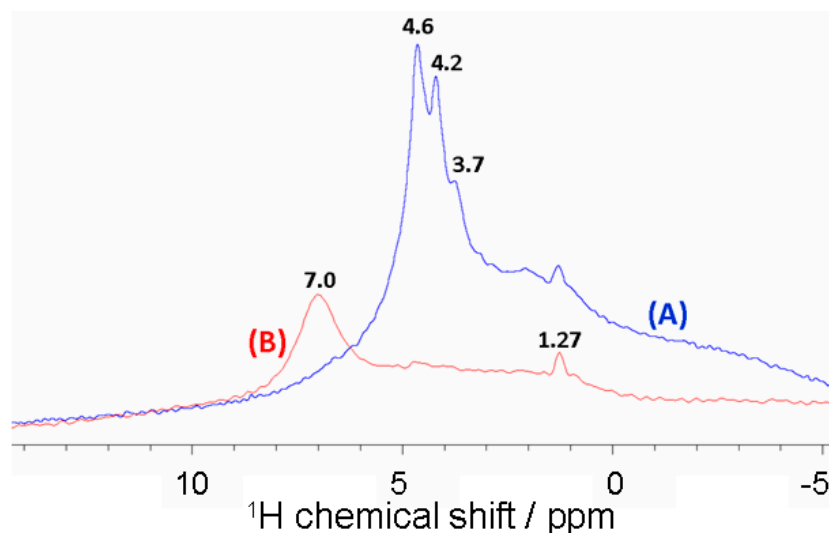
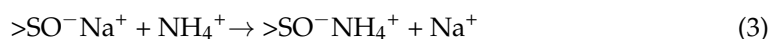


Figure 5. ^1H MAS NMR spectra of alkali-activated brick aggregates before (A) and after ammonium treatment (B).

After the addition of an NH_4Cl solution ($[\text{NH}_4\text{Cl}] = 0.5 \text{ mol}\cdot\text{L}^{-1}$) into a treated-brick suspension, the ^1H MAS NMR spectrum of the recovered material revealed that zeolitic protons shifted significantly to a lower field (Figure 5B). A single resonance appeared at $\delta = 7.0 \pm 0.1$ and was assigned to NH_4^+ ions which were adsorbed onto the Brønsted sites of the treated brick, leading to NH_4^+ -zeolite complexes [51–53]. As for Na^+ ions adsorbed onto treated brick, ^{23}Na MAS NMR analysis indicated their near disappearance after NH_4Cl treatment, confirming the involvement of an ion-exchange reaction between sodium(I) and ammonium(I) at the brick-water interface according to an equimolar heterogeneous process (Figure 6):



Note that the residual ^{23}Na signals observed in Figure 6B might be due to structural sodium bound to other brick minerals.

On the other hand, in order to generate the H-form of zeolites, alkali-activated brick was acidified progressively at a pH value close to 5 with an HCl solution ($[\text{HCl}] = 10^{-3} \text{ mol}\cdot\text{L}^{-1}$). This pH value was chosen lower than the pH at the point of zero charge, PZC ($\text{pH}_{\text{PZC}} = 5.85$) or the pH at the iso-electric point ($\text{pH}_{\text{IEP}} = 5.9$), see Figure S1, indicating the predominant occurrence of positively charged brick surfaces associated with hydroxonium ions. Acidified brick samples were afterward analyzed by ^1H and ^{23}Na MAS NMR spectroscopy. The ^1H MAS NMR spectrum of the acidified brick revealed the presence of a sharp peak at $\delta = 4.7$ ppm ascribed to H_3O^+ ions bound to brick zeolites, see Figure 7A. This signal was indeed due to hydrogen nuclei in bridging (structural) hydroxyl groups that underwent a rapid exchange between water molecules and hydroxonium ions in zeolitic cages. Such an observation agreed noticeably well with previous studies about the formation of hydroxyl groups in the low-silica zeolite with $n_{\text{Si}}/n_{\text{Al}} = 1$ (during the exchange of Na^+ cations by ammonium ions), particularly showing close signals in the chemical shift range of 3.6–4.8 ppm due to $\text{Si}(\text{OH})\text{Al}$ groups in the α and β -cages [54]. The resonance at $\delta_{1\text{H}} = 4.70$ ppm was also found to be similar enough to that observed in the spectra of X and Y zeolites and ascribed to $\text{Si}(\text{OH})\text{Al}$ groups in sodalite cages [52,55].

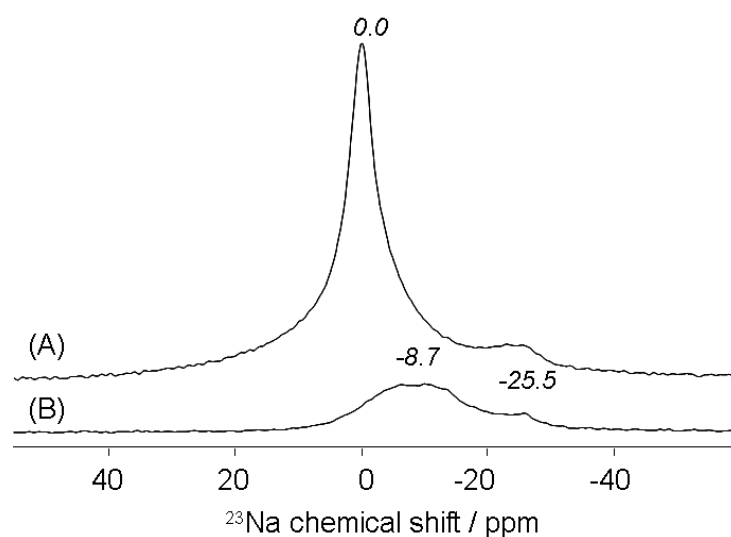


Figure 6. ^{23}Na MAS NMR spectra of zeolitized-brick samples before (A) and after ammonium treatment (B).

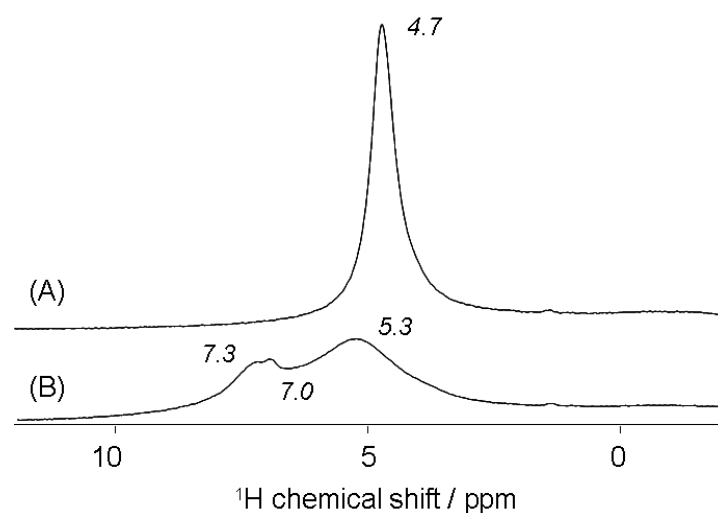


Figure 7. ^1H MAS NMR spectra of the acidified alkali-brick at pH 5 before (A) and after ammonium treatment (B).

Acidified alkali-brick was subsequently treated with an NH_4Cl solution ($[\text{NH}_4\text{Cl}] = 0.5 \text{ mol}\cdot\text{L}^{-1}$). The ^1H MAS NMR spectrum of the recovered sample displayed three new proton resonances (Figure 7B). The peaks at $\delta_1 \cong 7.3 \text{ ppm}$ and $\delta_1' = 7.0 \text{ ppm}$ were assigned both to NH_4^+ ions adsorbed onto Brønsted sites of framework zeolites: LTA and NaP (note that the δ_1 and δ_1' peaks were not yet assigned to specific zeolites). Whereas the peak at $\delta_2 = 5.3 \text{ ppm}$ was attributed to ammonium species involved in fast exchanges with NH_4^+ (δ_1 and δ_1') and hydroxonium ions in excess. A comparable magnetic phenomenon was already evidenced for other zeolites [56,57]. Moreover, by rotating the rotor at a higher speed (from 20 kHz to 60 kHz), the temperature of the rotor increased noticeably, which contributed to affecting the magnetic characteristics of the sample. The obtained ^1H MAS NMR spectrum then exhibited a line broadening and ^1H NMR signals merging, see Figure 8. This could be explained by hydrogen nuclei that underwent a rapid exchange between ammonium and hydroxonium ions. This suggested the possibility of a transfer of all four hydrogen nuclei from one ammonium ion to bridging hydroxyl groups. The small number of water molecules in the treated brick should also contribute to an increase in the mobility of ^1H nuclei along bridging $\text{Si}-\text{O}^- - \text{Al}$ chains. The resulting merging signal was centered at $\delta_3 = 5.07 \text{ ppm}$. Note that the weak resonance detected at the lower field in the ^1H MAS

NMR spectrum ($\delta_1'' = 6.75$ ppm) was still ascribed to the own protons of ammonium ions directly bound to bridging Si–O[−]–Al sites (as Si–O[−]–NH₄⁺–Al).

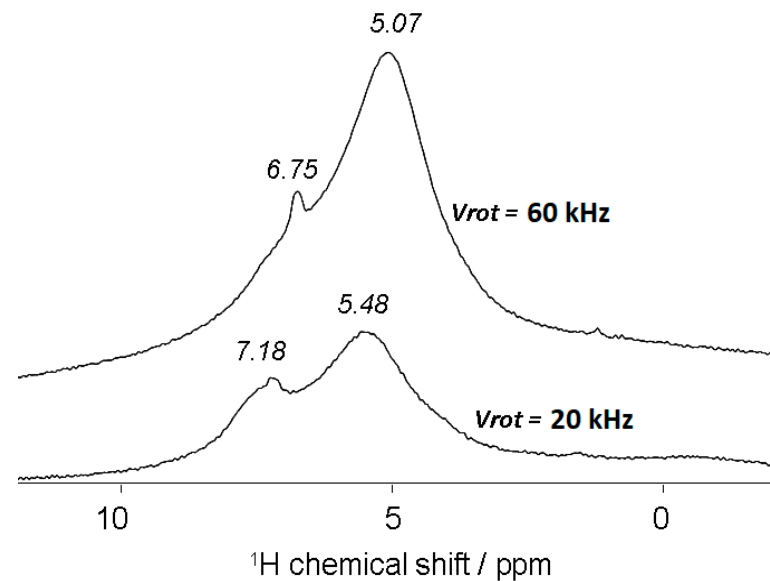


Figure 8. Magnetic field effects of the rotor speed on the ¹H MAS NMR spectrum of alkali-brick grains recovered after their acidification (pH 5) and ammonium treatment.

It could then be contended that upon H₃O⁺/NH₄⁺ exchange, the resonance of zeolitic ¹H nuclei were low-field-shifted by $\Delta\delta_1 = 2.45$ ppm (from 4.70 to ~7.15) and $\Delta\delta_2 = 0.60$ ppm (from 4.70 to 5.30), which globally reflected an increasing acid strength of brick protons. Such low-field-shifts induced by ammonium ions were previously observed in ¹H Solid-state NMR studies of Brønsted acid sites of other zeolites [52,53,56,57] and flame-derived silica/alumina [51] in which silanols with neighboring aluminum atoms generated bridging AlOHSi groups. However, it is worth noting that ¹H, ²³Na and ²⁷Al MAS NMR analyses permitted to reveal a progressive decomposition of brick zeolites as the medium pH decreased below 5 (see Figure S2).

3.3.3. ²⁷Al MAS NMR

Figure 9 displays solid-state MAS NMR data for ²⁷Al nuclei in alkali brick before and after NH₄Cl treatment. Globally, dominating ²⁷Al resonances observed for studied brick samples fall in the range $\delta = 59.0$ – 63.6 ppm. Such chemical-shift variations in the local environment of ²⁷Al(IV) within alkali-brick might suggest that Al(IV) sites would exist in distinct aluminosilicate frameworks and would be differentially affected by structural factors, i.e., bond angles/lengths in T–O–T, with T = Si or Al [14,58].

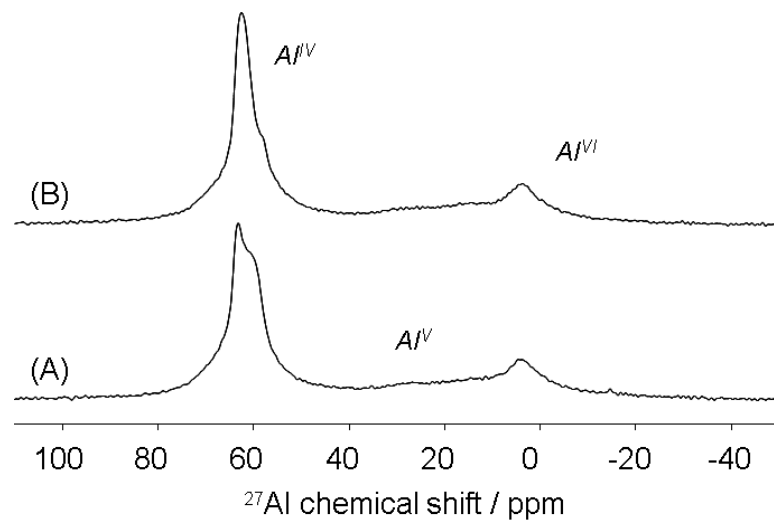


Figure 9. ^{27}Al MAS NMR spectra of alkali-brick samples before (A) and after ammonium treatment (B).

In the ^{27}Al MAS NMR spectrum of an alkali-brick sample, most aluminum atoms are tetrahedrally coordinated (Al^{IV}), which results in three ^{27}Al MAS NMR signals, see Figure 10A. The particular NMR resonances detected in the chemical shift range 57–61 ppm (see Figure 10A) were partially attributed to tetrahedrally coordinated aluminum (bound via oxygen to four ^{29}Si atoms to give $\text{Al}(\text{OSi})_4$ units) of both NaA and NaP zeolites [34,59–65].

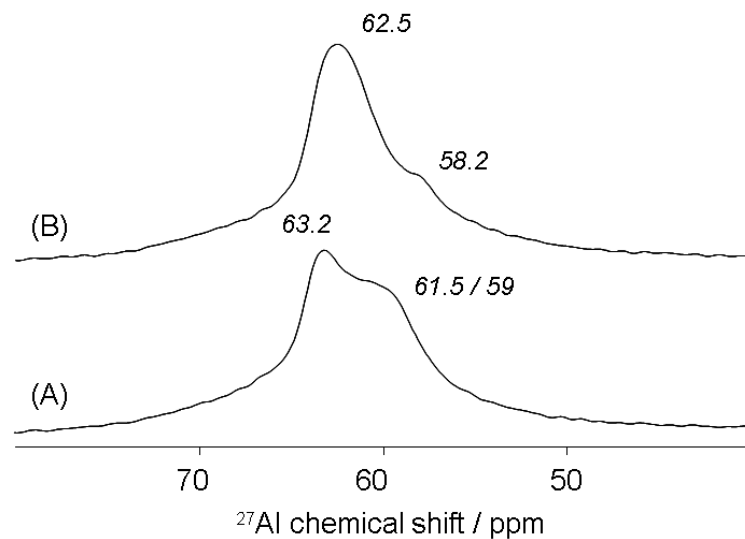


Figure 10. Detailed MAS NMR spectra of $^{27}\text{Al}^{\text{IV}}$ nuclei of alkali brick before (A) and after ammonium treatment (B).

According to the literature [34,63–65], a slightly lower chemical shift (about 1 ppm) in the $\delta^{27}\text{Al}$ range 57.6–59.3 ppm was more expected for NaP than for NaA. As for the NMR resonance at 63.2 ppm (see Figure 10A), it was ascribed to tetrahedrally coordinated aluminum in geo-polymeric gels, which were not transformed into zeolites [66]. Note that, for a series of sodalites ($\text{Si}/\text{Al} = \text{I}$), Jacobsen et al. (1989) [67] observed a linear dependence of ^{29}Si and ^{27}Al chemical shifts on mean “Si–O–Al” bond angles (θ):

$$\delta(^{29}\text{Si}) = -0.702 \cdot (\theta) + 11.626 \quad (4)$$

$$\delta(^{27}\text{Al}) = -0.724 \cdot (\theta) + 163.982 \quad (5)$$

From Equation (4), we attempted to calculate the mean Si–O–Al angle for brick hydroxyl-sodalite(s) (BS) with a ^{29}Si chemical shift $\delta(^{29}\text{Si}) = -84.5$ ppm (see Figure 4).

We found: $\theta_{BS} = 136.93^\circ$. This angle value permitted us to subsequently estimate the corresponding chemical shift of ^{27}Al nuclei in BS by using Equation (5). We found $\delta(^{27}\text{Al}) = 64.83$ ppm. This value was nevertheless higher than that observed experimentally: $\delta(^{27}\text{Al})_{\text{exp.}} = 63.2$ ppm. In contrast, by using Lippmaa et al.'s formulae (Equation (6); [68]) indicating the linear dependence of the ^{27}Al chemical shift on the mean [Al–O–Si] bond angle in framework aluminosilicates, we found a $\delta(^{27}\text{Al})$ value: $\delta(^{27}\text{Al}) = 63.53$ ppm, which was much closer to the experimental one.

$$\delta(^{27}\text{Al}) = -0.50 \cdot (\theta) + 132 \text{ (ppm)} \tag{6}$$

As for ^{29}Si nuclei of aluminosilicate gel(s) detected at -89.2 ppm (which superimposed on those of NaA and NaP zeolites), -94 ppm and -100.7 ppm, these chemical shifts would correspond to $\text{Q}^4(3\text{Al})$, $\text{Q}^4(2\text{Al})$ and $\text{Q}^4(1\text{Al})$ units, respectively; According to Ramdas-Klinowski's works [69], the ^{29}Si chemical shifts of brick gels could be correlated linearly with the structural parameter, $\sum d_{\text{TT}}$, according to:

$$\delta(^{29}\text{Si}) = 143.03 - 20.34 \cdot (\sum d_{\text{TT}} / \text{\AA}) \tag{7}$$

in which $\sum d_{\text{TT}}$ is defined as:

$$\sum d_{\text{TT}} = [3.37 \times m + 3.24 \times (4 - m)] \sin(\theta/2) \tag{8}$$

where m is the number of aluminum atoms in the $\text{Si}(m\text{Al})$ unit (in this study, $m = 1, 2, 3$). Using Equations (7) and (8), one could evaluate the mean Si–O–Al angle ($T = \text{Si}$ or Al) in the framework aluminosilicate. We found $\theta = 141.2^\circ$, 140.4° and 142.0° respectively for $\text{Q}^4(3\text{Al})$, $\text{Q}^4(2\text{Al})$ and $\text{Q}^4(1\text{Al})$ units of brick gel(s), see Table 3.

Table 3. Chemical shifts, $\delta(^{29}\text{Si})$ of ^{29}Si nuclei of the different $\text{Q}^4(m\text{Al})$ units present in modified-brick frameworks.

	$\text{Q}^4(4\text{Al})$ (in Gel)	$\text{Q}^4(4\text{Al})$ (in Zeolite)	$\text{Q}^4(3\text{Al})$ (in Gel)	$\text{Q}^4(2\text{Al})$ (in Gel)	$\text{Q}^4(1\text{Al})$ (in Gel)
Alkali-activated brick aggregates					
$\delta(^{29}\text{Si})$	-84.5	-89.2	-89.2	-94.0	-100.7
$\text{SiOAl}(\text{Si}), \theta^\circ$ ($\delta(^{27}\text{Al})$)	142.2 (60.9)	148.8 (57.6)	140.4 (61.8)	140.4 (61.8)	142.0 (61.0)
NH_4^+-loaded alkali-brick					
$\delta(^{29}\text{Si})$	-84.5	-89.7	-89.7	-94.6	-101.5
$\text{SiOAl}(\text{Si}), \theta^\circ$ ($\delta(^{27}\text{Al})$)	~ 139 (~ 62.5)	147.6 (58.2)	~ 139 (~ 62.5)	~ 139 (~ 62.5)	~ 139 (~ 62.5)

From these angle values, it was possible to assess the corresponding chemical shifts of ^{27}Al nuclei present in the different $\text{Q}^4(m\text{Al})$ units of brick gel(s) by employing Equation (6). We found $\delta(^{27}\text{Al}) = 61.4$ ppm, 61.8 ppm and 61.0 ppm for $\text{Q}^4(3\text{Al})$, $\text{Q}^4(2\text{Al})$ and $\text{Q}^4(1\text{Al})$ units of brick gel(s), respectively. These $\delta(^{27}\text{Al})$ values were consistent with the broad NMR resonances ranging from ~ 59 to ~ 61.5 ppm, which were observed in the ^{27}Al MAS NMR spectrum of alkali-brick (see Figure 10A). Likewise, the mean Si–O–Al angle ($T = \text{Al}$) in framework zeolites of alkali-brick was evaluated from Equations (7) and (8): we found: $\theta = 148.8^\circ$ for zeolitic $\text{Q}^4(4\text{Al})$ units (see Table 3); the corresponding chemical shift of ^{27}Al nuclei present in these $\text{Q}^4(4\text{Al})$ units was determined from Lippmaa et al.'s expression (Equation (6) [68]): $\delta(^{27}\text{Al}) = 57.6$ ppm. Also, from Engelhardt et al.'s expression (Equation (9) [43]), the mean Si–O–Al angle ($T = \text{Al}$) in framework zeolites of alkali brick

could be estimated ($\theta = 147.3^\circ$): in this case, the corresponding chemical shift value of ^{27}Al nuclei ($\delta(^{27}\text{Al}) = 58.3$ ppm) was found to be slightly higher than that determined above.

$$\delta(^{29}\text{Si}) = -0.570 \cdot (\theta) - 5.230 \quad (9)$$

A weak signal observed at 3.7 ppm was attributed to the presence of a small amount of octahedrally coordinated aluminum (Al^{VI}). ^{27}Al nuclei corresponding to penta-coordinated aluminum (Al^{V}) were also present inside alkali-brick networks and gave rise to a signal at approximately $\delta \cong 20\text{--}30$ ppm.

After NH_4Cl treatment, the ^{27}Al MAS NMR spectrum of the recovered material changed noticeably in comparison with that of the alkali-brick (Figures 9 and 10). The incorporation of NH_4^+ ions at high concentration into the alkali-brick suspension strongly displaced alkali cations (Na^+) from the extra-framework sites and fulfilled the charge balancing role (as shown in Figure 6 relative to the $\text{Na}^+/\text{NH}_4^+$ exchange at the brick surface). As observed by ^{27}Al MAS NMR (Figure 10B), the addition of ammonium to alkali-brick frameworks led to a broader signal at 62.5 ppm as a consequence of an overlapping of the $^{27}\text{AlO}_4$ resonances in the range $\sim 59\text{--}63$ ppm with an increase in the full width at half height (FWHH). This might be explained by the fact that the interactions of NH_4^+ ions with $\text{Q}^4 \text{AlO}_4$ sites of aluminosilicate gel(s) would contribute to a decreasing relaxation of the distortional bonding strain around Al^{IV} atoms. Such strains would lead to a shortening of Al–O bonds with improved tetrahedral symmetry when compared to Al bonding strains caused by H-bondings between Al sites and a water-sodium(I) mixture [70]. To support this, we reported here some relevant findings regarding protons' effects on the environment of silicon and aluminum framework atoms of aluminosilicates [71]. The authors in reference [71] concluded that the removal of protons from double four-membered rings (D4R: being present in sodalite structures) led to a strengthening of Si–O and Al–O bonds (and thereby a decrease of their lengths). In the resulting anionic framework, the Si–O–Al angle (138.4°) became larger (by 7.3°) than that at the bridging hydroxyl site (131.1°). In addition, in Section 3.3.2, it was shown that the adsorption of NH_4^+ ions onto alkali-brick resulted in acidification of brick particles, as evidenced by the significant shifting towards lower field observed by ^1H MAS NMR (see Figure 7B). This finding implied that similar decreases of Si–O–Al angles should exist in framework brick aluminosilicates from the anionic material ($>\text{SO}^-\text{Na}^+$) to the (pseudo)-protonated form, $>\text{SO}^-\text{H}_3\text{O}^+\text{NH}_3$, as previously suggested [51–53,56,57]. In this assumption, the mean Si–O–Al angles of NH_4^+ -loaded alkali-brick were evaluated by using Lippmaa et al.'s formulae, Equation (6). "Si–O–Si(Al)" angles data showed that: (i) the mean Si–O–Al angle in alkali-brick (148.8°) would be slightly higher (by 1.1°) than that at bridging hydroxyl sites of "protonated" alkali-brick (147.6°). As for aluminosilicate gels, the decrease of the mean Si–O–Al angle should range from $\sim 1^\circ$ to $\sim 3^\circ$.

3.3.4. 2D MAS NMR ($^{27}\text{Al}\text{--}\{^1\text{H}\}$) D-HMQC

In order to observe $^{27}\text{Al}\text{--}^1\text{H}$ dipolar-mediated correlations, 2D $^{27}\text{Al}(^1\text{H})$ D-HMQC experiments were performed on ammonium-loaded H-form of alkali-brick. As shown in Figure 11, two correlations were observed in the two-dimensional $^{27}\text{Al}(^1\text{H})$ D-HMQC spectrum: one between ^1H nuclei of NH_4^+ ($\delta_{^1\text{H}} = 7.0$ ppm) and Al^{IV} ($\delta_{^{27}\text{Al}} \cong 64$ ppm); and the other between ^1H nuclei of H_3O^+ ($\delta_{^1\text{H}} = 3.7$ ppm) and Al^{IV} ($\delta_{^{27}\text{Al}} \cong 62$ ppm).

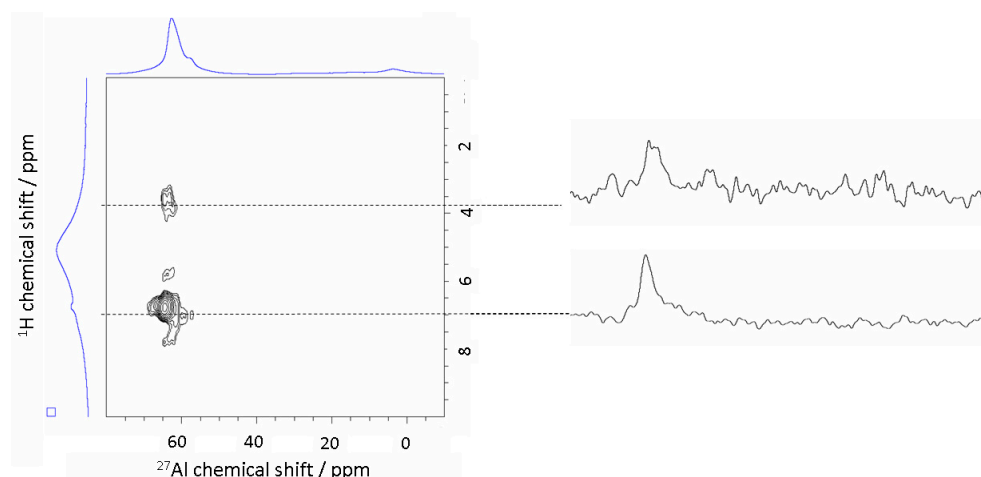


Figure 11. Observation of ^{27}Al – ^1H dipolar-mediated correlations from 2D $^{27}\text{Al}(^1\text{H})$ D-HMQC experiments performed on the ammonium-loaded H-form of alkali brick.

The observation of an $\text{Al}^{\text{IV}}\text{--NH}_4^+$ cross-peak in Figure 11 at (64, 7.0) ppm suggested that Brønsted acid sites Si--OH--Al , with Al^{IV} atoms were able to transfer protons of bridging hydroxyl groups to ammonia molecules. This chemical surface transfer led to a significant low-field shift of the ^1H NMR signal, as already observed previously for different types of zeolites [52,53,56,57]. Moreover, the ^1H MAS NMR signal reached a maximal intensity at about 5 ppm. At this resonance maximum, some of the NH_4^+ ions were involved directly in fast exchanges with ammonia adsorbed onto Brønsted sites ($\delta = 7.0$ ppm) and hydroxonium partially present in the H-form of brick zeolites ($\delta = 3.7$ ppm). Such an NH_4^+/H^+ exchange on brick surfaces indicated that not all bridging hydroxyl groups were involved in the signal at low field (i.e.: $\delta_{1\text{H}} = 7.0$ ppm). This could be explained by the fact that the hydrogen-exchange rate between ^1H nuclei of bridging hydroxyl sites and the four hydrogen nuclei of the ammonium ions became close to that relative to the chemical exchange of bridging hydroxyl groups between the sites. Such mixing exchanges then gave rise to a merging signal which occurred at a higher field shift (and therefore at a lower acidity strength) than that observed for ammonia interacting directly with negatively-charged bridging hydroxyl sites ($\text{Si--O}^- \text{--Al}$ groups), as suggested by Wang and his co-workers [53]. Note that by using ^1H MAS NMR and by rotating the rotor at different speeds, the transfer of hydrogen nuclei from ammonium ions to bridging hydroxyl groups was evidenced above (in Section 3.3.2 and Figure 8).

3.4. Aqueous Structural Stability and Cationic Immobilization Characteristics

In order to assess acidity effects on the aqueous structural stability of the brick composite at room temperature, a series of leaching tests were carried out at the following medium pH values: 0.39, 0.63, 0.80, 1.09, 1.27, 1.40, 1.67, 2.15, 2.32, 2.51, 3.70, 4.35 and 4.83. After a leaching time of 4 hours, the amounts of brick elements (Si, Al and Na) leached from the brick composite were determined and represented in the histogram of Figure 12. As seen in this figure, there are some noticeable differences between the leaching patterns of framework elements (Al and Si) and that of the extra-framework element (Na) with medium acidification. The concentrations of Al and Si present in the leachates remained low at reaction pH values above 2.5, suggesting a relative acid stability of the aluminosilicate matrix. Conversely, sodium was released at high concentrations with increasing acidification, revealing a facile exchange of Na^+ ions by H_3O^+ ions during leaching. This was in agreement with recent thermodynamic data revealing weak acid characteristics of Brønsted acid sites in aluminosilicate frameworks of alkali-activated brick [29]. At pH values below 2.5, the acid degradation of the brick composite occurred strongly, and hence the concentrations of Al, Si and Na in the leachates became important (Figure 12).

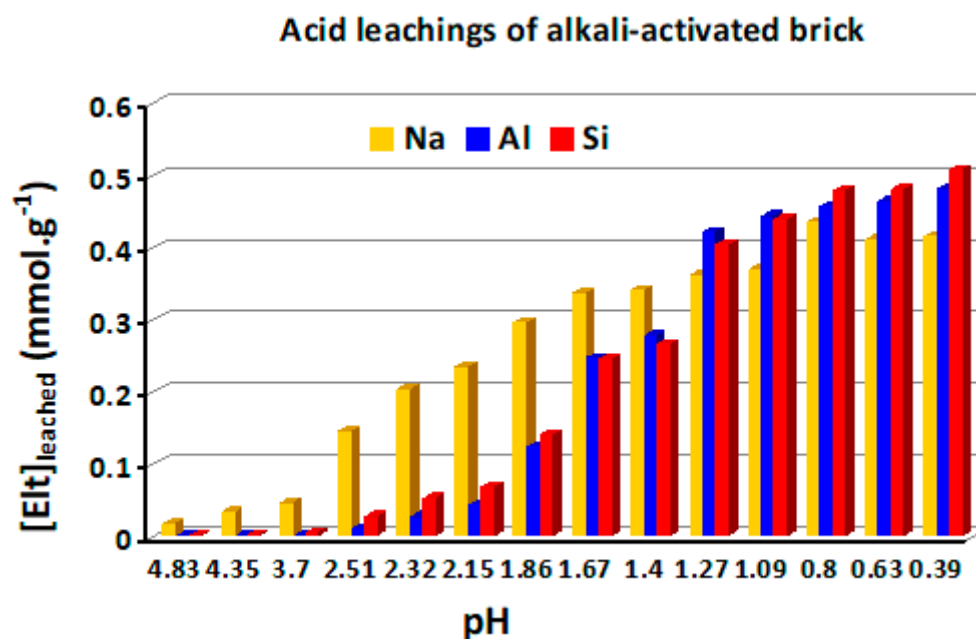


Figure 12. Histogram representing the evolution of the amounts of Na, Al and Si released in the leachates during the acid leaching of the brick-based composite at room temperature and reaction pH values ranging from 0.39 to 4.83.

On the other hand, the equilibrium reactions between the Na-exchanged forms of the brick composite and aqueous solutions containing one, two or three cationic metals, such as Cd^{2+} , Fe^{2+} , Ni^{2+} and Pb^{2+} (Me^{2+}), were previously studied thermodynamically on the basis of both the general properties of divalent metals in water and the global (zeolitic and geo-polymeric) surface characteristics of alkali-brick [46]. These investigations clearly revealed the importance of first hydrated radius, ionic potential and hydration-free energy, and second kinetics and mass-transfer/diffusion on the course of the global ion-exchange process at the brick–water interface [46]. Moreover, thermodynamic calculations concerning interfacial $2\text{Na}^+/\text{Me}^{2+}$ ion-exchange reactions revealed that the replacement of the exchangeable cation (Na^+) on the composite by Me^{2+} ions in the solution occurred favorably [46]. This proved that the immobilization efficiency of the composite for cationic metals is better than for Na^+ ions. To support this, acid leaching of alkali-brick samples doped with radio-active cations (Cs^+ and Rb^+) was carried out in a 0.01 M HCl solution (pH~2) at room temperature and under limited acid conditions close to material decomposition (as shown in Figure 13).

As expected, the concentrations of Al, Si, Na and radioactive elements in the leachates were found to be relatively high as a result of the acid degradation of the brick composite. By using the same leaching procedure, we afterward leached brick-composite samples which were previously calcined at 600 °C and 1000 °C for 4 h. Leaching results obtained at 600 °C indicated two features: (i) the leach fractions of Al and Si decreased noticeably, showing a slightly increased stability of calcined material; and (ii) the amounts of Na^+ , Cs^+ and Rb^+ (as extra-framework monovalent cations, M^+) in the leachates diminished as well, showing a positive effect on M^+ immobilization. This relative (weak) immobilization could be explained by the loss of water molecules in hydrated cationic shells during calcination, enabling the transformation of outer-sphere " $\text{M}(\text{H}_2\text{O})_x^+$ -brick" complexes into inner-sphere " M^+ -brick" complexes (as evidenced by MAS NMR, Boughriet et al., unpublished works). As for leaching results obtained at 1000 °C, they revealed that the concentrations of Al, Si, Na, Cs and Rb present in the leachate became very low, evidencing both a greater stabilization of the brick matrix and a strong immobilization of Na^+ , Cs^+ and Rb^+ ions, as already observed for alkali-activated (geo-polymerized) blast furnace slag/fly ash [3,13,72]. This latter point suggested that Na^+ , Cs^+ and Rb^+ ions were presumed to be encapsulated

inside a material that was structurally modified by heating, as previously mentioned for fly ash-silica fume-based geo-polymers after their calcination [13]. However, more studies on the brick-based composite must be undertaken to gain relevant information about structural/crystalline modifications induced by high temperatures.

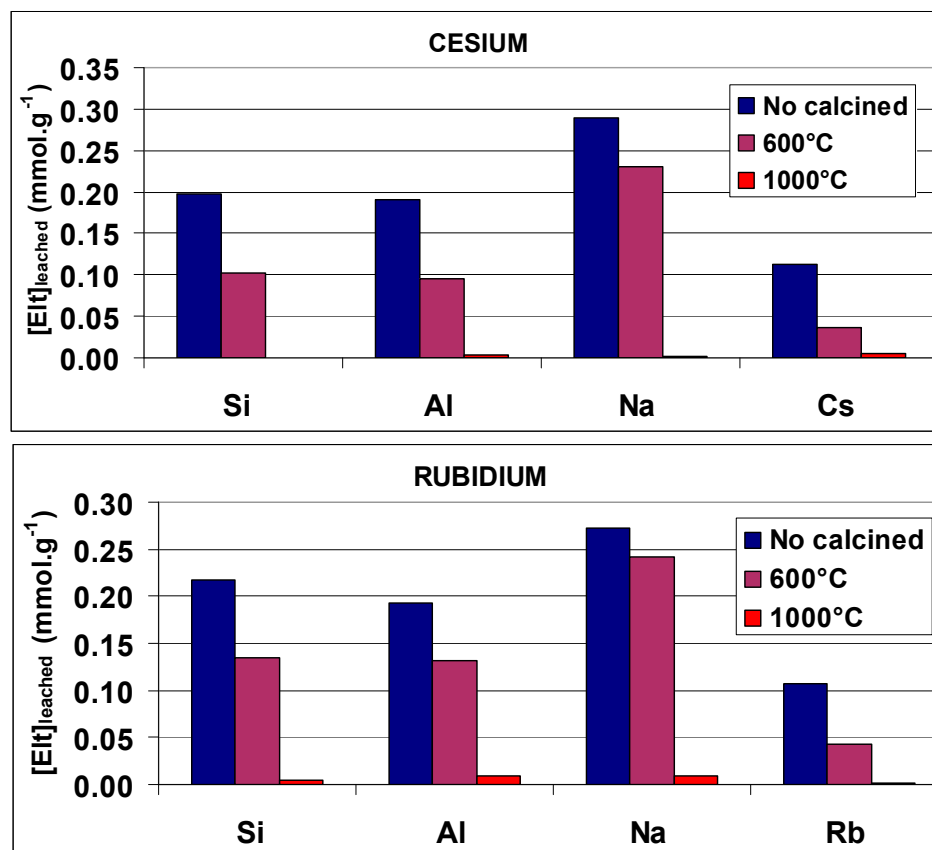


Figure 13. Histograms representing the evolution of the amounts of Si, Al, Na and Cs (or Rb) released in the leachates during the acid leaching (at pH 2 and room temperature) of the composite no-calcined and calcined at 600 °C and 1000 °C for 4 h.

4. Conclusions

The brick material was treated with sodium hydroxide using careful temperature control, giving rise to a geo-polymerization followed by a progressive zeolitization of geo-polymeric gels. X-ray diffraction analysis revealed the formation of crystalline structures identified as low-silica zeolites (NaA and NaP). ESEM/EDS microscopic analysis permitted observation of the cubic and spherical specimens at the brick surface and the evaluation of their averaged elemental composition, thus confirming the occurrence of low-silica zeolites with atomic ratios Si/Al close to 1. Solid MAS NMR spectroscopy permitted us to obtain a comprehensive insight into the different ^{29}Si , ^{27}Al and ^1H nuclei environments existing in brick-composite networks. ^{29}Si and ^{27}Al MAS RMN studies revealed the still existence of geo-polymerized gels in combination with low-silica zeolites and allowed an estimation of the “geo-polymeric silicon” contribution inside the studied material. ^1H MAS NMR studies showed the existence of bridging $\text{Si}-\text{O}^- - \text{H}_3\text{O}^+ - \text{Al}$ chains and their implication in rapid exchanges with hydrogen nuclei of water molecules and ammonium ions. Protons transfer from ammonium to bridging $\text{Si}-\text{O}^- - \text{Al}$ sites was confirmed by using two-dimensional $^{27}\text{Al}(^1\text{H})$ D-HMQC NMR. Detailed spectral analyses of ^1H , ^{29}Si and ^{27}Al NMR resonances allowed the assessment of “Si-O-Si(Al)” angles. Structural angle calculation permitted us to evidence the effects of extra-framework cations (Na^+ , H_3O^+ and NH_4^+) on negatively-charged bridging hydroxyl sites ($\text{Si}-\text{O}^- - \text{Al}$ groups).

Acid-leaching tests revealed that heating treatment was an effective method to stabilize the significant composite structure, as well as to improve the immobilization of radio-active elements (Cs and Rb).

5. Future Prospects

Alkali-activated brick represents a novel alkali-activated binder on which negative surface charges represent potential immobilization sites for radio-active cationic species. Geo-polymers and low-silica zeolites would be considered interesting binding phases for radio-elements uptake. The low Si/Al ratio in these compounds contributed to high adsorption density that would facilitate ionic exchanges between Na^+ ions at the solid surface and radioactive ions (Cs^+ , Rb^+ , Sr^{2+} and Co^{2+}) in the solution. However, a comprehensive insight into interfacial phenomena must still be clarified on the basis of kinetics and thermodynamics investigations. The knowledge obtained here on the compositional, structural and interfacial (ionic) properties of brick-based composite would help: (i) to interpret the interfacial ion exchange; (ii) to understand the uptake and leaching mechanism of radioactive ions; and (iii) to ensure better nuclear waste immobilization and nuclear radiation shielding after calcination/vitrification.

Pyrolysis–Fourier transform infrared (Py-FTIR) spectrometric studies of alkali-brick at elevated temperatures are in prospect for understanding the pyrolysates composition and their evolution over time and analyzing the difference between Na and H form geo-polymer. In addition, studies are underway to evaluate the state of the immobilized radio-elements and their degree of encapsulation inside composite frameworks after calcination at different temperatures. For that, X-ray photoelectron spectroscopy (XPS) should be useful for etching matrix surfaces by ionic Ar^+ bombardment at different durations and analyzing surface elements versus formed-crater depth.

Supplementary Materials: The following supporting information can be downloaded at: <https://www.mdpi.com/article/10.3390/ceramics6030108/s1>, Figure S1: determination of the point of zero charge and isoelectric point of alkali brick; Figure S2 (a) (^1H): ^1H MAS NMR spectra of alkali-brick grains vs medium pH; (b) (^{27}Al): ^{27}Al MAS NMR spectra of alkali-brick grains vs medium pH; (c) (^{23}Na): ^{23}Na MAS NMR spectra of alkali-brick grains vs medium pH; Figure S3: ESEM images of alkali-brick grains. Quantitative ESEM/EDS analyses performed on: large zones of surface aggregates (~300–500 μm)—(A); zeolites-rich zones(50–60 μm)—(B); different targeted ‘zeolitic’ particles—(C).

Author Contributions: Conceptualization: A.B., O.A., G.T., B.R. and M.W.; methodology: A.B., O.A., N.P., G.D. and M.W.; formal analysis: A.B., O.A., N.P., G.D., G.T., B.R., B.O. and M.W.; investigation: A.B., O.A., G.T., B.R. and M.W.; resources: A.B., O.A., B.O. and M.W.; data curation: A.B., O.A., G.T., B.R. and M.W.; writing—original draft preparation: A.B.; writing—review and editing: A.B.; supervision: A.B., O.A., B.O. and M.W.; project administration: B.O. and M.W.; funding acquisition: M.W. All authors have read and agreed to the published version of the manuscript.

Funding: This research received no external funding.

Institutional Review Board Statement: Not applicable.

Informed Consent Statement: Not applicable.

Data Availability Statement: The authors confirm that the data supporting the findings of this study are available within the article.

Acknowledgments: Scientific works were undertaken successfully owing to the cooperation between the University of Lille (France) and the University of Bangui (Central African Republic). This collaboration (being still underway) and the Grant-in-Aid to Gildas Doyemet for his Doctoral-Thesis preparation is financially supported by the Embassy of France to Bangui. Financial support from the IR INFRANALYTICS FR2054 for conducting the research is gratefully acknowledged. The Region “Hauts de France” and the French government are warmly acknowledged for the co-funding of these apparatus. Scanning electron microscopy studies were undertaken in the laboratory UMR LOG 8187 at the Department of Earth Sciences (Villeneuve d’Ascq 59655, France). The authors gratefully thank Sandra Vantalon (Chemical Engineer) for carrying out careful ESEM/EDS analyses.

Conflicts of Interest: The authors declare no conflict of interest.

References

1. Pierrehumbert, R. There is no Plan B for dealing with the climate crisis. *Bulletin At. Sci.* **2019**, *75*, 215–221. [[CrossRef](#)]
2. Glasser, F. Application of inorganic cements to the conditioning and immobilisation of radioactive wastes. In *Handbook of Advanced Radioactive Waste Conditioning Technologies*; Ojovan, M.I., Ed.; Woodhead Publishing: Sawston, UK, 2011; pp. 67–135.
3. Komljenovića, M.; Tanasijevića, G.; Džunuzovića, N.; Provis, J.L. Immobilization of cesium with alkali-activated blast furnace slag. *J. Hazard. Mater.* **2020**, *388*, 121765. [[CrossRef](#)]
4. Li, Q.; Sun, Z.; Tao, D.; Xu, Y.; Li, P.; Cui, H.; Zhai, J. Immobilization of simulated radionuclide $^{133}\text{Cs}^+$ by fly ash-based geopolymer. *J. Hazard. Mater.* **2013**, *262*, 325–331. [[CrossRef](#)]
5. Deng, N.; An, H.; Cui, H.; Pan, Y.; Wang, B.; Mao, L.; Zhai, J. Effects of gamma-ray irradiation on leaching of simulated $^{133}\text{Cs}^+$ radionuclides from geopolymer wasteforms. *J. Nucl. Mater.* **2015**, *459*, 270–275. [[CrossRef](#)]
6. Kuenzel, C.; Cisneros, J.F.; Neville, T.P.; Vandeperre, L.; Simons, S.J.R.; Bensted, J.; Cheeseman, C.R. Encapsulation of Cs/Sr contaminated clinoptilolite geopolymers produced from metakaolin. *J. Nucl. Mater.* **2015**, *466*, 94–99. [[CrossRef](#)]
7. Jang, J.G.; Park, S.M.; Lee, H.K. Physical barrier effect of geopolymeric waste form on diffusivity of cesium and strontium. *J. Hazard. Mater.* **2016**, *318*, 339–346.
8. Wagh, A.S.; Sayenko, S.Y.; Shkuropatenko, V.A.; Tarasov, R.V.; Dykiy, M.P.; Svitlychniy, Y.O.; Virych, V.D.; Ulybkina, E.A. Experimental study on cesium immobilization in struvite structures. *J. Hazard. Mater.* **2016**, *302*, 241–249. [[CrossRef](#)]
9. Al-Jubouri, S.M.; Curry, N.A.; Holmes, S.M. Hierarchical porous structured zeolite composite for removal of ionic contaminants from waste streams and effective encapsulation of hazardous waste. *J. Hazard. Mater.* **2016**, *320*, 241–251. [[CrossRef](#)]
10. Arbel Haddad, M.; Ofer-Rozovsky, E.; Bar-Nes, G.; Borjovich, E.J.C.; Nikolski, A.; Mogiliansky, D.; Katz, A. Formation of zeolites in metakaolin-based geopolymers and their potential application for Cs immobilization. *J. Nucl. Mater.* **2017**, *493*, 168–179. [[CrossRef](#)]
11. El-Naggar, M.R.; Amin, M. Impact of alkali cations on properties of metakaolin and metakaolin/slag geopolymers: Microstructures in relation to sorption of ^{134}Cs radionuclide. *J. Hazard. Mater.* **2018**, *344*, 913–924. [[CrossRef](#)]
12. Vandevenne, N.; Iacobescu, R.I.; Pontikes, Y.; Carleer, R.; Thijssen, E.; Gijbels, K.; Schreurs, S.; Schroeyers, W. Incorporating Cs and Sr into blast furnace slag inorganic polymers and their effect on matrix properties. *J. Nucl. Mater.* **2018**, *503*, 1–12. [[CrossRef](#)]
13. Tian, Q.; Nakama, S.; Sasaki, K. Immobilization of cesium in fly ash-silica fume based geopolymers with different Si/Al molar ratios. *Sci. Total Environ.* **2019**, *687*, 1127–1137. [[CrossRef](#)]
14. Walkley, B.; Ke, X.; Hussein, O.H.; Bernal, S.A.; Provis, J.L. Incorporation of strontium and calcium in geopolymer gels. *J. Hazard. Mater.* **2020**, *382*, 121015. [[CrossRef](#)]
15. Ojovan, M.I.; Lee, W.E. *Immobilisation of Radioactive Waste in Cement in: An Introduction to Nuclear Waste Immobilisation*, 2nd ed.; Elsevier: Oxford, UK, 2014; Chapter 15; pp. 205–232.
16. Park, B.; Kim, J.; Ghoreishian, S.M.; Rethinasabapathy, M.; Suk Huh, Y.; Kang, S.-M. Generation of multi-functional core-shell adsorbents: Simultaneous adsorption of cesium, strontium and rhodamine B in aqueous solution. *J. Ind. Eng. Chem.* **2022**, *112*, 201–209. [[CrossRef](#)]
17. Jiang, C.; Ni, J.; Jin, G.P. Magnetic potassium cobalt hexacyanoferrate nanocomposites for efficient adsorption of rubidium in solution. *Sep. Purif. Technol.* **2022**, *296*, 121383. [[CrossRef](#)]
18. Almas Dutt, M.; Asif Hanif, M.; Nadeem, F.; Bhatti, H.N. A review of advances in engineered composite materials popular for wastewater treatment. *J. Environ. Chem. Eng.* **2020**, *8*, 104073. [[CrossRef](#)]
19. Roshanfekar Rad, L.; Anbia, M. Zeolite-based composites for the adsorption of toxic matters from water: A review. *J. Environ. Chem. Eng.* **2021**, *9*, 106088. [[CrossRef](#)]
20. Li, J.; Xu, Z.; Li, L.; Li, H.; Hu, D.; Xiang, Y.; Han, L.; Yu, Y.; Ning, L.; Peng, X. Short communication on 'Incorporating radionuclide Sr into geopolymer-zeolite A composites: Geopolymerisation characteristics. *J. Nucl. Mater.* **2022**, *563*, 153625. [[CrossRef](#)]
21. Yang, S.; Yang, L.; Gao, M.; Bai, H.; Nagasaka, T. Synthesis of zeolite-geopolymer composites with high zeolite content for Pb (II) removal by a simple two-step method using fly ash and metakaolin. *J. Clean. Prod.* **2022**, *378*, 134528. [[CrossRef](#)]
22. Dehou, S.C.; Wartel, M.; Recourt, P.; Revel, B.; Mabingui, J.; Montiel, A.; Boughriet, A. Physicochemical, crystalline and morphological characteristics of bricks used for ground waters purification in Bangui region (Central African Republic). *Appl. Clay Sci.* **2012**, *59*, 69–75. [[CrossRef](#)]
23. Poumaye, N.; Allahdin, O.; Tricot, G.; Revel, B.; Billon, G.; Recourt, P.; Wartel, M.; Boughriet, A. MAS NMR investigations on a metakaolinite-rich brick after zeolitization by alkaline treatments. *Microporous Mesoporous Mater.* **2019**, *277*, 1–9. [[CrossRef](#)]
24. Massiot, D.; Fayon, F.; Capron, M.; King, I.; Le Calvé, S.; Alonso, B.; Durand, J.-O.; Bujoli, B.; Gan, Z.; Hoatson, G. Modelling one- and two-dimensional solid-state NMR spectra. *Magn. Reson. Chem.* **2002**, *40*, 70–76. [[CrossRef](#)]
25. Gan, Z. $^{13}\text{C}/^{14}\text{N}$ heteronuclear multiple-quantum correlation with rotary resonance and REDOR dipolar recoupling. *J. Magn. Reson.* **2007**, *184*, 39–43. [[CrossRef](#)]
26. Tricot, G.; Trébosc, J.; Pourpoint, F.; Gauvin, R.; Delevoye, L. The D-HMQC MAS-NMR Technique. In *Annual Reports on NMR Spectroscopy*; Webb, G.A., Ed.; Elsevier Ltd.: Amsterdam, The Netherlands, 2014; Volume 81, pp. 145–184. [[CrossRef](#)]
27. Poumaye, N.; Allahdin, O.; Wartel, M.; Boughriet, A. Insights into characterization and adsorptive behaviour of zeolitized brick in water toward cadmium (A very toxic heavy metal to humans). *Int. J. Pharm. Pharmaceut. Res.* **2018**, *13*, 1–29.

28. Poumaye, N.; Allahdin, O.; Lesven, L.; Wartel, M.; Boughriet, A. Adsorption of Iron (II) on Sodic Zeolites-Bearing Brick (In Batch): Insights into Interfacial Chemical Processes and Thermodynamic Equilibria. *Int. J. Sci. Res. Methodol.* **2019**, *11*, 88–119.
29. Boughriet, A.; Allahdin, O.; Poumaye, N.; Tricot, G.; Revel, B.; Lesven, L.; Wartel, M. Micro-Analytical Study of a Zeolites/Geo-Polymers/Quartz Composite, Dielectric Behaviour and Contribution to Brønsted Sites Affinity. *Ceramics* **2022**, *5*, 908–927. [[CrossRef](#)]
30. Allahdin, O.; Wartel, M.; Recourt, P.; Revel, B.; Ouddane, B.; Billon, G.; Mabingui, J.; Boughriet, A. Adsorption capacity of iron oxyhydroxide-coated brick for cationic metals and nature of ion surface interactions. *Appl. Clay Sci.* **2014**, *90*, 141–149. [[CrossRef](#)]
31. Seliem, M.K.; Komarneni, S. Equilibrium and kinetic studies for dissociation of iron from aqueous solution by synthetic Na-A zeolites: Statistical modelling and optimization. *Microporous Mesoporous Mater.* **2016**, *228*, 266–274. [[CrossRef](#)]
32. Tontisirin, S. Synthesis and characterization of co-crystalline zeolite composite of LSX/A. *Microporous Mesoporous Mater.* **2017**, *239*, 123–129. [[CrossRef](#)]
33. Sathupunya, M.; Glari, E.; Wongkasemjit, S. ANA and GIS zeolite synthesis directly from alumatrane and silatrane by sol-gel process and microwave technique. *J. Eur. Ceram. Soc.* **2002**, *22*, 2305–2314. [[CrossRef](#)]
34. Zubowa, H.-L.; Kosslick, H.; Müller, D.; Richter, M.; Wilde, L.; Fricke, R. Crystallization of phase-pure zeolite NaP from MCM-22-type gel compositions under microwave radiation. *Microporous Mesoporous Mater.* **2008**, *109*, 542–548. [[CrossRef](#)]
35. Behin, J.; Kazemian, H.; Rohani, S. Sonochemical synthesis of zeolite NaP from clinoptilolite. *Ultrason. Sonochem.* **2016**, *28*, 400–408. [[CrossRef](#)]
36. Treacy, M.M.J.; Higgins, J.B. *Collection of Simulated XRD Powder Patterns for Zeolites*, 5th ed.; Elsevier: New York, NY, USA, 2007; pp. 1–762. [[CrossRef](#)]
37. Gao, X.; Yu, Q.L.; Brouwers, H.J.H. Apply ^{29}Si , ^{27}Al MAS NMR and selective dissolution in identifying the reaction degree of alkali activated slag-fly ash composites. *Ceram. Int.* **2017**, *43*, 12408–12419. [[CrossRef](#)]
38. Lippmaa, E.; Mägi, M.; Samoson, A.; Tarmak, M.; Engelhardt, G. Investigation of the structure of zeolites by solid-state high-resolution ^{29}Si NMR spectroscopy. *J. Am. Chem. Soc.* **1981**, *103*, 4992–4996. [[CrossRef](#)]
39. Hunger, M.; Anderson, M.W.; Ojo, A.; Pfelfer, H. Study of the geometry and location of the bridging OH groups in aluminosilicate and silicoaluminophosphate type zeolites using ^1H MAS NMR sideband analysis and CP/MAS NMR. *Microporous Mater.* **1993**, *1*, 17–32. [[CrossRef](#)]
40. Fernandez-Jimenez, A.; Monzo, M.; Vicent, M.; Barba, A.; Palomo, A. Alkaline activation of metakaolin-fly ash mixtures: Obtain of Zeoceramics and Zeocements. *Microporous Mesoporous Mater.* **2008**, *108*, 41–49. [[CrossRef](#)]
41. Criado, M.; Fernandez-Jimenez, A.; Palomo, A.; Sobrados, I.; Sanz, J. Effect of the $\text{SiO}_2/\text{Na}_2\text{O}$ ratio on the alkali activation of fly ash. Part II: ^{29}Si MAS-NMR Survey. *Microporous Mesoporous Mater.* **2008**, *109*, 525–534. [[CrossRef](#)]
42. Souayfan, F.; Rozière, E.; Paris, M.; Deneele, D.; Loukili, A.; Justino, C. ^{29}Si and ^{27}Al MAS NMR spectroscopic studies of activated metakaolin-slag mixtures. *Constr. Build. Mater.* **2022**, *322*, 126415. [[CrossRef](#)]
43. Engelhardt, G.; Luger, S.; Buhl, J.C.; Felsche, J. ^{29}Si MAS n.m.r. of aluminosilicate sodalites: Correlations between chemical shifts and structure parameters. *Zeolites* **1989**, *9*, 182–186. [[CrossRef](#)]
44. Duxson, P.; Provis, J.L.; Lukey, G.C.; Separovic, F.; van Deventer, J.S.J. ^{29}Si NMR study of structural ordering in aluminosilicates geopolymer gels. *Langmuir* **2005**, *21*, 3028–3036. [[CrossRef](#)]
45. Ortega-Zavala, D.E.; Burciaga-Díaz, O.; Escalante-García, J.I. Chemically bonded ceramic/cementitious materials of alkali activated metakaolin processed by cold pressing. *Constr. Build. Mater.* **2021**, *279*, 121365. [[CrossRef](#)]
46. Allahdin, O.; Poumaye, N.; Wartel, M.; Boughriet, A. Correlation analysis between cationic metal characteristics and ion-exchange performance of brick-derived zeolites: A comprehensive mechanistic explanation. *Mater. Chem. Phys.* **2022**, *276*, 125353. [[CrossRef](#)]
47. Engelhardt, G.; Michel, D. *High-Resolution Solid-State NMR of Silicates and Zeolites*; Wiley & Sons: London, UK, 1987; p. 485, ISBN 0471915971.
48. MacKenzie, K.J.D.; Smith, M.E. Multinuclear Solid-State NMR of Inorganic Materials. *Pergamon Mater. Ser.* **2002**, *6*, 727.
49. Lin, H.; Liu, H.; Li, Y.; Kong, X. Properties and reaction mechanism of phosphoric acid activated metakaolin geopolymer at varied curing temperatures. *Cem. Concr. Res.* **2021**, *144*, 106425. [[CrossRef](#)]
50. Engelhardt, G. Multinuclear solid-state NMR in silicate and zeolite chemistry. *TrAC Trends Anal. Chem.* **1989**, *8*, 343–347. [[CrossRef](#)]
51. Huang, J.; van Vegten, N.; Jiang, Y.; Hunger, M.; Baiker, A. Increasing the Brønsted acidity of flame-derived silica/alumina up to zeolitic strength. *Angew. Chem.* **2010**, *122*, 7942–7947. [[CrossRef](#)]
52. Jiang, Y.; Huang, J.; Dai, W.; Hunger, M. Solid-state nuclear magnetic resonance investigations of the nature, property, and activity of acid sites on solid catalysts. *Solid State Nucl. Magn. Reson.* **2011**, *39*, 116–141. [[CrossRef](#)]
53. Wang, C.; Dai, W.; Wu, G.; Guan, N.; Li, L. Application of ammonia probe-assisted solid-state NMR technique in zeolites and catalysis. *Magn. Reson. Lett.* **2022**, *2*, 28–37. [[CrossRef](#)]
54. Dyballa, M.; Obenaus, U.; Lang, S.; Gehring, B.; Traa, Y.; Koller, H.; Hunger, M. Brønsted sites and structural stabilization effect of acidic low-silica zeolite A prepared by partial ammonium exchange. *Microporous Mesoporous Mater.* **2015**, *212*, 110–116. [[CrossRef](#)]
55. Huang, J.; Jiang, Y.; Reddy Marthala, V.R.; Wang, W.; Sulikowski, B.; Hunger, M. In situ ^1H MAS NMR investigations of the H/D exchange of alkylaromatic hydrocarbons on zeolites H-Y, La, Na-Y, and H-ZSM-5. *Microporous Mesoporous Mater.* **2007**, *99*, 86–90. [[CrossRef](#)]

56. Ma, D.; Han, X.; Xie, S.; Bao, X.; Hu, H.; Au-Yeung, S.C.F. An investigation of the roles of surface aluminum and acid sites in the zeolite MCM-22. *Chem. Eur. J.* **2002**, *8*, 162–170. [[CrossRef](#)]
57. Kanellopoulos, J.; Gottert, C.; Schneider, D.; Knorr, B.; Prager, D.; Ernst, H.; Freude, D. NMR investigation of proton mobility in zeolites. *J. Catal.* **2008**, *255*, 68–78. [[CrossRef](#)]
58. Ruiz-Santaquiteria, C.; Skibsted, J.; Fernández-Jiménez, A.; Palomo, A. Alkaline solution/binder ratio as a determining factor in the alkaline activation of aluminosilicates. *Cem. Concr. Res.* **2012**, *42*, 1242–1251. [[CrossRef](#)]
59. Glid, M.; Sobrados, I.; Ben Rhaïem, H.; Sanz, J.; Ben Haj Amara, A. Alkaline activation of metakaolinite-silica mixtures: Role of dissolved silica concentration on the formation of geopolymers. *Ceram. Int.* **2017**, *43*, 12641–12650. [[CrossRef](#)]
60. Miladinovic, Z.P.; Zakrzewska, J.; Kovacevic, B.T.; Miladinovic, J.M. In situ ^{27}Al NMR kinetic investigation of zeolite A crystallization. *Microporous Mesoporous Mater.* **2014**, *195*, 131–142. [[CrossRef](#)]
61. Kulshreshtha, S.K.; Vijayalakshmi, R.; Sudarsana, V.; Salunke, H.G.; Bhargava, C. Iron oxide nanoparticles in NaA zeolite cages. *Solid State Sci.* **2013**, *21*, 44–50. [[CrossRef](#)]
62. Xiao, Y.; Sheng, N.; Chu, Y.; Wang, Y.; Wu, Q.; Liu, X.; Deng, F.; Meng, X.; Feng, Z. Mechanism on solvent-free crystallization of NaA zeolite. *Microporous Mesoporous Mater.* **2017**, *237*, 201–209. [[CrossRef](#)]
63. Albert, B.R.; Cheetham, A.K.; Stuart, J.A.; Adams, C.J. Investigations on P zeolites: Synthesis, characterisation, and structure of highly crystalline low-silica NaP. *Microporous Mesoporous Mater.* **1998**, *21*, 133–142. [[CrossRef](#)]
64. Nery, J.G.; Mascarenhas, Y.P.; Cheetham, A.K. A study of the highly crystalline, low-silica, fully hydrated zeolite P ion exchanged with (Mn^{2+} , Cd^{2+} , Pb^{2+} , Sr^{2+} , Ba^{2+}) cations. *Microporous Mesoporous Mater.* **2003**, *57*, 229–248. [[CrossRef](#)]
65. Meftah, M.; Oueslati, W.; Chorfi, N.; Ben Haj Amara, A. Effect of the raw material type and the reaction time on the synthesis of halloysite based Zeolite Na-P1. *Result Phys.* **2017**, *7*, 1475–1484. [[CrossRef](#)]
66. Fletcher, R.A.; MacKenzie, K.J.D.; Nicholson, C.L.; Shimada, S. The composition range of aluminosilicate geopolymers. *J. Eur. Ceram. Soc.* **2005**, *25*, 1471–1477. [[CrossRef](#)]
67. Jacobsen, H.S.; Norby, P.; Bildsøe, H.; Jakobsen, H.J. 1:1 Correlation between ^{27}Al and ^{29}Si chemical shifts and correlations with lattice structures for some aluminosilicate sodalites. *Zeolites* **1989**, *9*, 491–495. [[CrossRef](#)]
68. Lippmaa, E.; Samoson, A.; Mägi, M. High-resolution ^{27}Al NMR of aluminosilicates. *J. Am. Chem. Soc.* **1986**, *108*, 1730–1735. [[CrossRef](#)]
69. Ramdas, S.; Klinowski, J. A simple correlation between isotropic ^{29}Si -NMR chemical shifts and T-O-T angles in zeolite frameworks. *Nature* **1984**, *308*, 521–523. [[CrossRef](#)]
70. O’Neil Parker, W., Jr.; SWegner, S. Aluminum in mesoporous silica–alumina. *Microporous Mesoporous Mater.* **2012**, *158*, 235–240. [[CrossRef](#)]
71. Limtrakul, J.; Tantanak, D. Cationic, structural, and compositional effects on the surface structure of zeolitic aluminosilicate catalysts. *Chem. Phys.* **1996**, *208*, 331–340. [[CrossRef](#)]
72. Jain, S.; Banthia, N.; Troczynski, T. Leaching of immobilized cesium from NaOH-activated fly ash-based geopolymers. *Cem. Concr. Compos.* **2022**, *133*, 104679. [[CrossRef](#)]

Disclaimer/Publisher’s Note: The statements, opinions and data contained in all publications are solely those of the individual author(s) and contributor(s) and not of MDPI and/or the editor(s). MDPI and/or the editor(s) disclaim responsibility for any injury to people or property resulting from any ideas, methods, instructions or products referred to in the content.